REPORT DOCUMENTATION PAGE

Form Approved
OMB No. 0704-0188

1. AGENCY USE ONLY *(Leave blank)*	2. REPORT DATE	3. REPORT TYPE AND DATES COVERED
		FINAL 01 SEP 93 TO 31 AUG 96

4. TITLE AND SUBTITLE
EXPERIMENTAL AND THEORETICAL ASPECTS OF CORROSION DETECTION AND PREVENTION

5. FUNDING NUMBERS
F49620-93-1-0565
61103D 3484/RS

6. AUTHOR(S)
W. R. MADYCH

AFOSR-TR-96
97
0007

7. PERFORMING ORGANIZATION NAME(S) AND ADDRESS(ES)
UNIVERSITY OF CONNECTICUT
DEPARTMENT OF MATHEMATICS
STORRS, CT 06269

9. SPONSORING/MONITORING AGENCY NAME(S) AND ADDRESS(ES)
AFOSR/NM
110 DUNCAN AVE, SUITE B115
BOLLING AFB DC 20332-8080

10. SPONSORING/MONITORING AGENCY REPORT NUMBER
F49620-93-1-0565

11. SUPPLEMENTARY NOTES

12a. DISTRIBUTION AVAILABILITY STATEMENT
APPROVED FOR PUBLIC RELEASE:
DISTRIBUTION UNLIMITED

12b. DISTRIBUTION CODE

13. ABSTRACT *(Maximum 200 words)*
SEE REPORT

14. SUBJECT TERMS

15. NUMBER OF PAGES

16. PRICE CODE

17. SECURITY CLASSIFICATION OF REPORT	18. SECURITY CLASSIFICATION OF THIS PAGE	19. SECURITY CLASSIFICATION OF ABSTRACT	20. LIMITATION OF ABSTRACT
UNCLASSIFIED	UNCLASSIFIED	UNCLASSIFIED	SAR

FINAL TECHNICAL REPORT

October 31, 1996

Experimental and theoretical aspects of corrosion detection and prevention

AFOSR Grant No. F49620-93-1-0565

Technical report no. 3

Principal investigator: W. R. Madych
Department of Mathematics, U-9
University of Connecticut
Storrs, CT 06269
Phone: 203-486-3923

Co-principal investigator: O. F. Devereux
Department of Metallurgy
Institute of Materials Science, U-136
University of Connecticut
Storrs, CT 06269

Report Summary

This report summarizes activities and work completed between September 1, 1993 and October 31, 1996. In addition to this summary it contains two parts consisting of various details.

The experimental portion of this project is supervised by O. F. Devereux and conducted by P. C. Su. As indicated in the earlier reports, it is devoted to the investigation of initiation and growth kinetics of corrosion in airframe alloys, including joined and protectively coated specimens. The goal is to understand fundamental mechanisms by which corrosion damage develops in order to assist in design, maintenance, and performance evaluation of airframe systems. The general investigative procedure is based on the principles of electrochemical impedance spectroscopy, EIS. These principles together with the problems which we address by this method have been outlined in the earlier reports and are succinctly summarized in the introduction to Part 1. The remainder of Part 1 is devoted to a detailed description of the work which was carried out. This work is also described in articles 7, 8, and 9 on the list of technical reports.

The theoretical portion concerns (i) the study of a mathematical model of corrosion conducted by G. Hernandez and (ii) investigation of certain algorithmic aspects of tomography and signal and image processing supervised by W. R. Madych.

The objective of (i) was to determine the theoretical consequences of a well known mathematical model of corrosion in alloys and the details of obtained results were summarized in article 1 on the list which was included in the second annual report.

The work associated with (ii) is detailed in articles 2, 3, 4, and 5 on the list. Articles 2, 3, and 4 were summarized and included in the first two annual reports. Article 5 concerns computed tomography, is contained in Part 2 of this report, and may be briefly described as follows: In order to approximate a small portion of a cross section conventional reconstruction algorithms require the averages over all lines which pass through the entire cross section. In this work we show how certain high frequency components of a portion

of a cross section can be approximated using only averages over lines which pass through or close to the region of interest. The resulting high frequency information is often sufficient for the detection of flaws, abnormalities, etc. Our method relies on the notions associated with the so-called continuous wavelet transform and the observation that Radon's classical formula is a summability formula with an integrable convolution type kernel. What is also significant is that our method can be numerically realized via simple modifications of well-established convolution-backprojection algorithms.

Technical Reports

1. G. E. Hernandez, Internal-external corrosion in alloys, tech. rep.

2. I. Koltracht, W. R. Madych, and K. Marinelli, Image magnification using families of fast orthogonal transforms, *Int. J. Imaging Systems and Technology*, Vol. 7, (1996), 170-179.

3. R. A. Lorentz and W. R. Madych, Translation and dilation invariant subspaces and multiresolution analyses, to appear in *Applied and Computational Harmonic Analysis.*

4. W. R. Madych, Finite orthogonal transforms and multiresolution analyses on intervals, to appear in *J. Fourier Analysis and Application.*

5. W. R. Madych, Reconstruction and wavelet transforms for quasilocal tomography, tech. rep. submitted for publication.

6. W. R. Madych, Wavelets and their applications, a guest editorial in *Int. J. Imaging Systems and Technology*, Vol. 7, (1996), 149-151.

7. P. C. Su, O. F. Devereux and W. Madych, Impedance Imaging For Prediction and Detection of Airframe Corrosion, in *Structural Integrity in Aging Aircraft*, C. I. Chang and C. T. Sun, eds., ASME AD-Vol. 47, pp. 247-251,

8. P. C. Su and O. F. Devereux, AC and DC Electrochemical Studies of A Lanolin-Based Inhibitor on 2024 Aluminum, submitted for publication in *Corrosion.*

9. P. C. Su and O. F. Devereux, Impedance Studies of the Corrosion of Painted and Jointed 2024 Aluminum, in preparation.

Articles 1, 2, 3, 4, and 7 together with suitable summaries have already been submitted with earlier technical reports to the AFOSR. The material in articles 8 and 9 is described in detail in the enclosed report by Devereux and Su in Part 1. Report 5 is enclosed in its entirety in Part 2.

Presentations

The following formal presentations where made by the investigators associated with this grant:

1. W. R. Madych, Impedance Imaging for Prediction and Detection of Airframe Corrosion, Second USAF Aging Aircraft Conference, Oklahoma City, Oklahoma, May, 1994. Report of work of P. C. Su, O. F. Devereux and W. R. Madych. Recorded in the proceedings edited by C. I. Chang.

2. W. R. Madych, Finite orthogonal transforms and multiresolution analyses on intervals. Tomography Meeting at the Mathematical Research Institute in Oberwolfach, Germany, Sept. 1994. Presentation of some of the results in article 4 listed above.

3. W. R. Madych, Image magnification using families of fast orthogonal transforms, Wavelet Meeting at the Mathematical Research Institute in Oberwolfach, Germany, July. 1995. Presentation of some of the results in article 2 listed above.

4. P. C. Su, Impedance Imaging for Prediction and Detection of Airframe Corrosion, San Francisco, Nov. 12-17, 1995. Presentation of results in the article 7 listed above.

5. O. F. Devereux, Detailed Modeling of AC and DC Laboratory Measurements for Corrosion Prediction at Ambient and Elevated Temperatures, NACE Mid-America Corrosion Conference, Chicago, Oct. 1-4, 1995. Report of work of K. S. Yeum and O. F. Devereux.

6. O. F. Devereux, Experimental and Theoretical Aspects of Corrosion Detection and Prevention, AFOSR NDE program review, Warner-Robins ALC, Robins AFB, April 2, 1996. Report of work of P. C. Su, O. F. Devereux and W. R. Madych.

7. W. R. Madych, Pointwise inversion of Radon transforms, Special session on Tomography, AMS Meeting in Lawrenceville, N. J., Oct. 1996. Discussed certain consequences of some of the results in article 5 listed above.

We mention that the principal investigator, W. R. Madych, was a guest editor for the special issue (Fall 1996) of the *International Journal of Imaging Systems and Technology* devoted to wavelets and their applications in image processing.

Part 1

INTRODUCTION

The Aging Aircraft Problem.

The aging aircraft problem, that of maintaining in service our military and civilian fleets for periods longer than their projected service life, has been recognized for some time. A broad view of the technological issues associated with this problem has been given recently by Chang, including understanding the corrosion processes that occur in aircraft, the detection of corrosion damage and the prevention of corrosion, and the understanding, detection, and prevention of damage due to mechanical processes such as fatigue.[1] These may be intertwined, as in the fatigue failure of structures weakened by corrosion.

The mechanisms by which corrosion occurs, or "the forms of corrosion," have been categorized in various ways;[2] those of particular interest to the aircraft problem include general corrosion, galvanic corrosion and crevice corrosion. All corrosion is electrochemical in nature and can be understood in terms of a galvanic cell. In general corrosion the structure is uniformly attacked by an oxidizing environment such as moist air. In galvanic corrosion dissimilar metals are involved; these exhibit different affinities for reducing agents in their environment (e.g., in moist neutral environments, dissolved oxygen) forcing on a metal to be cathodic (site of reduction) and the other to be anodic (site of oxidation). Unless the anode forms a highly protective oxide film by virtue of the corrosion process, it is attacked and dissolves in the environment. In crevice corrosion a restricted geometry, such as a riveted joint, creates a cell by virtue of the different environments within and without the crevice. Within the crevice the dissolving metal

hydrolyses to form a solid oxide, e.g. $Al(OH)_3$, which isolates the crevice, permitting the environment within the interior of the crevice to be different from the bulk medium exterior to the crevice. The act of hydrolyzing, e.g., $Al^{+3} + 3H_2O \Rightarrow Al(OH)_3 + 3H^+$, also acidifies the crevice, enhancing the solubility of the corrosion product and preventing formation of a protective oxide film, while the net positive charge in this region attracts the ubiquitous chloride ion, Cl^-, which further unstabilizes the protective oxide and accelerates the corrosion process. In applying these mechanisms to aircraft corrosion we must understand that aluminum alloys make up much of an aircraft's structure, that a mature aircraft may have, literally, thousands of pounds of brackish water within its structure, that aluminum is highly reactive and is stabilized only by a highly protective Al_2O_3 film which in turn is readily attacked by Cl^-, that aircraft structures are replete with crevices, such as those formed by riveted joints, and the use of steel fasteners in juxtaposition to aluminum, promoting galvanic corrosion, is commonplace. The detection of skin corrosion, i.e., that of areas of sheet aluminum, is being addressed by ultrasonic, x-ray diffraction and eddy current technology; the complex geometry of joints renders application of these techniques difficult at best, useless at worst.

Corrosion of Aluminum Alloys.

Aluminum and its alloys are generally somewhat resistant to general corrosion in near-neutral waters due to the highly stoichiometric and thus protective oxide film that will form spontaneously or via a deliberate process such as anodizing or chemical conversion. This film is, however, readily penetrated by chloride ion, causing pitting corrosion which proceeds by a mechanism somewhat akin to crevice corrosion. Pitting is

a cosmetic issue in aircraft, but may also become a structural issue through the creation of stress raisers. Aluminum is susceptible to crevice corrosion because of the acidification which occurs within the crevice geometry which prevents formation of protective oxide, and of the attraction of the ubiquitous and detrimental environmental chloride by the metal ions within the crevice. In galvanic couples involving brackish waters aluminum is more active, or anodic, than other common metals except for magnesium and zinc, but its galvanic behavior is not always predictable due to the extremely passive nature of its oxide film. Corrosion of aluminum beneath protective organic coatings is likely to occur in a manner somewhat analogous to crevice corrosion. Common aircraft alloys such as 2024 and 7075 are also subject to exfoliation corrosion, detectable by ultrasonic means, and to stress corrosion cracking. The latter mode of failure occurs in high strength materials in particular environments when the material is stressed above a critical level; it is commonly controlled in aircraft by assuring that service loads are maintained below the critical stress level.

Corrosion Preventive Inhibitor.

Corrosion preventive inhibitors are frequently used for protection of aircraft structures. Current corrosion preventive measures rely heavily upon inhibitor systems which use volatile solvent carriers, e.g., MIL-C-81309 [3], in which the active inhibitor is a petroleum sulfonate and which forms a soft "oil-like" film on the surface, and MIL-C-85054 [4], which has a similar base but also contains silicone and alkyd resins and cures to form a relatively hard film. In addition to the environmental liability of the

volatile organic carrier, these systems are not suitable for moving parts and afford only temporary protection, yet are difficult to remove.

Interest in new protection systems for aluminum alloys is motivated by concern for both improved protection of the aircraft and for the environment. In this work, the ability of a wool wax-based commercial inhibitor, Fluid Film® has been evaluated. Wool wax consists primarily of lanolin, whose major components are the esters RCOOR′ and R″COHCOOR′. It is environmentally benign, and is applied as a water-based emulsion, thereby avoiding liability of volatile organic solvents.

Electrochemical Impedance Spectroscopy in Corrosion Research.

The corrosion of a metal is an electrochemical process and involves the transport of both ions and electrons in the vicinity of the interface between the metal and an electrolytic environment. It has a resistive aspect, described by the field dependence of the anodic and cathodic reactions, and a capacitive aspect arising from a non-homogeneous distribution of ions and conduction electrons in the vicinity of the interface. Therefore, the behavior of a corroding metal can often be represented by the electrical behavior of a simple circuit comprised of resistors, capacitors and other simple elements such as shown in Figure 2 (a).

In Electrochemical Impedance Spectroscopy (EIS) a small AC signal (5-20 mv) is applied between the specimen, termed the working electrode, and an inert counterelectrode and the magnitude and phase of the resulting current is measured. From this information, the complex impedance of the interface can be determined over a range of frequencies, and values for components of a corresponding equivalent circuit can be

determined through fitting the impedance spectrum to the set of equations describing the model circuit via the use of software such as that developed by Boukamp.[5] Although EIS may be used to quantify corrosion rates over a broad range from the very fast to the vanishingly small, it is especially suited to systems which experience low corrosion rates, i.e., well-protected systems. In well-protected systems such as painted or anodized metals, the metal/electrolyte interface behaves as a resistor, R_p, and capacitor, C_c, in parallel, and the electrolyte behaves as a series resistor, R_s, such as in the model circuit shown in Figure 2 (b). The resistance R_p includes the corrosion rate of the metal and electronic leakage through the protective film, while the capacitance is that of the protective film and is frequently seen to reflect the diffusion of water into the film. As noted, interfaces are characterized by a non-uniform distribution of mobile charges, or "electrical double layer," which may be characterized as a capacitor, C_{dl}, in series with the film but may not be seen due to its typically large magnitude (capacitors in series add as reciprocals).

Degradation of protective coatings and corrosion of metal substrates can be assessed from changes of the values of equivalent circuit parameters determined through EIS. One advantage of EIS over traditional DC polarization is its non-destructive nature; the use of a small excitation signal permits determination of long-term corrosion properties without perturbing the system. Current computer-driven instrumentation renders this technique both user-friendly and rapid, and permits explicit evaluation of the individual electrical characteristics of even highly resistive interfaces such as well-protected airframe structures.

Research Plan.

This program has focused upon crevice corrosion in simulated aircraft structures as a critical mode of failure that is not adequately addressed by the more traditional NDT methods now under investigation. In addition, it has employed electrochemical methods in a study of the efficacy of lanolin-based inhibitors, with particular attention to crevice and to previously corroded structures.

EXPERIMENTAL OUTLINE

The aluminum alloy 2024-T3 with and without a MIL-P-23377+MIL-C-85285 epoxy primer and polyurethane topcoat system were being used in this study. These coated specimens were provided by the Navy Air Warfare Center, Patuxent River, Maryland, and were designed to meet the extremely corrosive service environment of Naval aircraft. Bare 2024-T3 aluminum specimens were polished to a 600 grit finish, washed with double distilled water and degreased with acetone. Inhibitor-coated specimens were prepared by applying the wool wax-based inhibitor, Fluid Film®, by brush, providing a weight gain after drying of ~9.5 mg/cm^2.

The impedance cell was a 2 in. dia., 4 in. high (5 cm ×10 cm) Pyrex® cylinder, sealed to the 3″×3″(7.5 cm × 7.5 cm) × 1.5 mm specimen via a Viton® O-ring, which provided an exposed specimen area of 18.3 cm^2. The cell contained a simulated service environment comprised of 150 cc of 0.5M NaCl in double distilled water. A crevice was simulated by affixing a Teflon® cap screw with a shoulder through the exposed surface of the specimen using a predetermined torque (160 inch ounces). The inhibitor-coated specimens were air-dried for three hours before assembling into the cell, which was open to the atmosphere to permit natural aeration. The aluminum specimen comprised the working electrode, the counterelectrode was a 316L stainless steel plate and the reference electrode was a saturated calomel electrode. Impedance spectra were obtained with a Solatron Model 1250 Frequency Response Analyzer coupled with a Solatron Model 1286 Potenstiostat and an on-line computer. Z-plot® software was used to control the

experiments, and equivalent circuit modeling was performed with Boukamp's **EQUICRT** software.[5]

Measurement of the open circuit potential and DC electrode polarization studies were also conducted in a glass cell with an air-purged 0.5M NaCl aqueous solution as the electrolyte, a 1 cm^2 2024-T3 disk as working electrode, a saturated calomel electrode as reference electrode, and a graphite rod as the counterelectrode. These experiments were performed with a Princeton Applied Research Potentiostat/Galvanostat Model 273 interfaced to a personal computer, using PAR 352 Corrosion Analysis Software and a polarization scan rate of 0.17mv/s.

PROGRAM ACCOMPLISHMENTS

A. Outline of Achievements.

The work performed under this contract consisted of a number of tasks:

1. Define the fundamental impedance response of the aluminum airframe alloys by performing baseline EIS measurements in saline environment; and determine the time dependence of corrosion in systems of interest via dynamic impedance analysis. **This task has been completed.**
2. Apply these methods to specific structures representative of airframe geometries, i.e., joined and protected coated specimens. **Aluminum specimens with simulated joint were studied in corrosive environment.**
3. Develop a methodology to distinguish between a corroding structure and an inert structure, e.g., between a sound riveted joint and a riveted joint undergoing hidden corrosive attack. **The extent to which the different structures have corroded can be determined from the corresponding type of equivalent circuit, and from the magnitude of the equivalent circuit parameters.**
4. Evaluate the effectiveness of a new eviromentally innocuous commercial inhibitor, "Fluid Film", with electrochemical techniques as an alternative for the protection of the aircraft structures from corrosion. **DC and AC electrochemical techniques have been applied; results indicate that the inhibitor can effectively protect aluminum from corrosion even if initial corrosion has already occurred.**

These results are described in the following pages:

B. Detail Tasks Summaries:

1. Baseline EIS response and time dependence of EIS behavior for 2024-T3 airframe aluminum alloy in saline environment.

Extensive EIS data have been collected on the aluminum alloy 2024-T3 immersed in aqueous 0.5M NaCl in the (a) as received, (b) painted, and (c) treated with a commercial wool waxed-based inhibitor conditions. These impedance spectra are well behaved and reproducible, and can be fit with, a high degree of accuracy to appropriate equivalent circuits. Typical Nyquist and Bode representations for bare aluminum are shown in Figure 1 (a) and (b); they are modeled with the Randles equivalent circuit, shown in Figure 2 (a), and the dependence of the equivalent circuit parameters with immersion is given in Table 1. In Randles circuit R_s represents a series or electrolyte resistance, C_{dl} is the capacitance of the double layer, R_{ct} is the charge transfer resistance, and W is the Warburg impedance, given by [6]

$$W=(\sigma/\omega^{1/2})(1-j)\tanh[h(j\omega/D)^{1/2}]$$

where ω is the circular frequency, σ is the "Warburg coefficient," h is the diffusion thickness and D is the relevant diffusivity.

Figure 3 (a) and (b) display impedance spectra for painted aluminum with an intact coating and damaged coating, respectively, and model curves using with the equivalent circuit shown in Figure 2 (b). These spectra display a effect of the presence of flaws in the coating as shown in Figure 3 (b). Such behavior may or may not be accompanied by a

visible blister or other artifact in the paint and in long term exposure tests is generally discernible via EIS prior to the appearance of any visible defect. The differences in these intact and damaged coatings is shown quantitatively via the effect on model circuit parameters in Figures 4 through 7. The coating capacitance, C_c, increases markedly during the first 30 days of exposure, Figure 4; this behavior is consistent with water uptake by the coating and is similar for the two specimens because this phenomenon is independent of damage. The step-like appearance of the capacitance is attributed to "non-Fickian" diffusion of water into the film caused by successive occupation of different types of site in the film by water. Figure 5 compares the film, or "pore," resistance of the damaged and intact paint, a parameter which reflects the DC conductivity of the paint. For the intact film this decrease in accord with the water adsorption shown in Figure 5; the damaged film displays a significantly lower resistance that rapidly deteriorates as major film flaws develop. Both parameters, C_c and R_{po}, thus quantitatively indicate degradation of protective coatings by physical damage, intrinsic defects or diffusive invasion. Figure 6 compares the polarization resistance of the metal substrate for the two coatings. This parameter is a direct measure of the resistance of the system to corrosion in that its reciprocal, $1/R_p$, is representative of corrosion rate. Polarization resistance gradually deteriorates with time in both systems, suggesting continued degradation after the coatings become saturated with water; and R_p is significantly lower for the damaged system, indicative of very little protection. The variation in the double layer capacitance with exposure time shown in Figure 7 is marked. Initially very low, the value of C_{dl} for the intact coating increases by nearly three orders of magnitude to approximately 5

$\mu F/cm^2$. The increase in this parameter with time indicates the development of an ionic space charge within the paint film; the much larger values seen for the damaged film represents actual contact of water with the metal.

2. EIS study of jointed and protected aluminum airframe structures.

Extensive testing similar to that performed on simple specimens has been performed on a structural model comprised of the painted Al 2024-T3 with a simulated rivet, i.e., a stepped nylon cap screw affixed to the test plate with a predetermined torque, to provide a reproducible, defined crevice geometry without introducing the artifact of a galvanic couple. Figure 8 (a) and (b) depict Nyquist and Bode representation of the EIS of such a joint over a month of immersion in 0.5M NaCl. The short term behavior is similar to that of the simple specimen of Figure 3 with two time constants displayed, but upon exposure the impedance decreases indicating a region of weaker protection associated with the crevice which appears, however, to be stable.

With a riveted joint displaying visible corrosion, shown in Figure 9 (a) and (b), we see a marked reduction in impedance magnitude, but also a characteristic third time constant which appears to represent a region of active corrosion within the crevice. The equivalent circuit of Figure 2 (c) was used to model the corroding crevice. Figure 10 illustrates the comparison of corroding and non-corroding joints; for the corroding crevice, the impedance value after 4 days immersion in the test electrolyte is already much smaller than that of the non-corroding crevice after 36 days immersion. Circuit parameters for corresponding to the corroding joint in Figure 9 are shown in Figure 11 and Figure 12. The coating capacitance, C_c, and the double layer capacitance, C_{dl}, both increase with time, this can be attributed to the water diffusion into the coating as with case of the coated sample. The crevice-related capacitance, C_{cv}, increases with time up to 30 days then decreases. The capacitance values associated with the corroding crevice are

abnormally high (~mF/cm^2). Such large capacitance values have been interpreted as "supercapacitance",[7] and may be associated with Faradaic (or corrosive) processes at the surface which mimic the charging characteristics of a capacitor, or as a "pseudocapacitance" [8] which may be associated with an electrosorption process. The pore resistance, R_{po}, and the polarization resistance, R_p, both decrease with immersion time as with the simple coated specimens. The crevice-related resistance, R_{cv}, may be related to the charge transfer resistance of the crevice and displays relatively small values which decrease with immersion time, suggesting minimum corrosion protection. It has been reported that the pH value of the fluid within the crevice for neutral dilute sodium chloride solution is near 2,[2] highly solubilizing to the protective oxide layer on aluminum. Tests of macro specimens in similar solutions confirm the role of the crevice environment in facilitating corrosion. The equivalent circuit parameters for bare 2024-T3 in 0.5M NaCl aqueous solution pH 2 are shown in Table 2, Comparing R_{ct} values in Table 1 with those in Table 2, the charge transfer resistance in the acidic environment is at least 10 times smaller than that in neutral solution. Thereby, the EIS technique allows us to discern the extent of corrosion in joined and protected aluminum structures, and the presence of an actively corroding crevice can be clearly detected in contrast to other techniques.

3. Methodology to differentiate a corroded structure from a sound structure.

In the previous task 1, we showed that the degree of protection afforded by a coating on an aluminum structure can be quantified by the EIS technique in terms of the magnitude of equivalent circuit parameters such as C_c and R_{ct} before any visual degradation is appeared. Through task 2, hidden corrosion such as crevice corrosion in a fabricated structure was shown to be detected by the analysis of equivalent circuit parameters, C_{cv} and R_{cv} obtained via EIS. Thereby, if equivalent circuit analysis are obtained with EIS data from an in-service structure, information about the condition of the structure with respect to existing corrosive damage can be easily determined.

4. Apply electrochemical techniques to evaluate the effectiveness of an environmentally innocuous corrosion inhibitor on airframe aluminum alloy.

The variation of open circuit potential (OCP) with immersion time for as-polished and inhibitor-coated specimens is shown in Figure 13. The OCP of the bare specimen drops from the initial value of -610 mV SCE and approaches a nearly steady value of -740 mV SCE after ~20 h. The bare sample specimen shows considerable fluctuation in OCP value between 5 and 15 hours of immersion, suggestive of vigorous initial pitting activity that latter stabilizes.[9] The initial decrease of the OCP of the bare sample is consistent with an increase of the average anodic current due to rapid localized dissolution rates at pits sites, with the subsequent steady value indicative of a stable pit structure. The OCP of the inhibitor-coated aluminum increases monotonically with immersion time and approaches a steady state, indicative of an absence of pitting and suggestive of a diminishing anodic reaction rate. This would be expected if the inhibitor film encourages a slow but uniform, i.e., pit-free, growth of aluminum oxide.

Polarization curves for bare 2024-T3 aluminum in aerated 0.5M aqueous NaCl and for inhibitor-coated 2024-T3 aluminum in the same environment are displayed in Figure 14. The corrosion potential of bare aluminum is higher than that of the inhibitor-coated aluminum, and corresponds to the OCP upon initial immersion in Figure 13. The current densities for bare aluminum are about 4 orders of magnitude larger than those for coated aluminum, indicative of the protective nature of this inhibitor.

Polarization data for the bare and the coated aluminum electrodes were analyzed via the modeling technique of Yeum and Devereux,[10, 11] and are shown in Figures 15 and 16, respectively, together with model curves. In this model the polarization potential is

the sum of the potentials attributable to electron transfer (activation) polarization, diffusion (concentration polarization), and ohmic drop in the electrolyte. For the jth reaction this is expressed as:

$$i_j = s_j(1-s_j i_j/i^s_j)^{m_j} \exp[s_j(V-V^*_j)/b_j]\exp(-iAR_j/b_j)$$

where s_j is +1 for an anodic reaction and -1 for a cathodic reaction, i^s_j is the limiting diffusion current, m_j is the reaction order, $2.303b_j$ is the Tafel slope, A is the surface area of the electrode and R is the cell resistance. The defined parameter V^*_j combines the functions of the equilibrium potential and the exchange current and is given by

$$V^* = V_{ref} - s_j b_j \ln(z_j \Im k_j) - s_j b_j \ln(\prod_{i=1}^{nj} a_i^{m_i})$$

where V_{ref} represents the potential of the reference electrode relative to the electrolyte, z_j is the number of electrons transferred in the rate controlling step, $\Im$ is the Faraday, k_j is the chemical rate constant, and the a_i are the activities of the reacting species. The total current experienced by the electrode is the sum of the currents carried by the individual reactions:

$$i = | \sum_{j=1}^{nj} i_j |$$

The technique utilizes a nonlinear regression procedure to optimize the values of the model parameters.

The polarization curve for bare 2024-T3 aluminum in aerated 0.5M NaCl, Figure 15, is modeled by three reactions: C2, reduction of hydrogen ion, modeled by electron

transfer polarization and ohmic drop; C1, reduction of dissolved oxygen, modeled by electron transfer polarization and diffusion; and A1, anodic oxidation of aluminum, modeled by electron transfer polarization and ohmic drop. Although the model can incorporate passivation there was no evidence of passive behavior, perhaps due to the almost immediate onset of chloride-induced pitting. Model parameters for these reactions are listed in Table 3; the corrosion current, from the model, is 0.104 mA/cm^2.

The polarization curve for inhibitor-coated 2024-T3 aluminum in aerated 0.5M NaCl, Figure 16, is modeled by two reactions: C1, reduction of dissolved oxygen, and A1, anodic oxidation of aluminum, both controlled by electron transfer polarization and diffusion. Model parameters for these reactions are listed in Table 4; the corrosion current, from the model, is 9.35 nA/cm^2, four orders of magnitude smaller than that of bare aluminum.

Impedance spectra were recorded after various times of immersion in naturally aerated, aqueous 0.5M NaCl; Nyquist and typical Bode plots are shown for inhibitor-coated specimens in Figure 17 (a) and (b). Historically, various equivalent circuit models have been used to model impedance spectra of inhibitor-coated aluminum,[12, 13] e.g., two RC elements in series or in parallel, with and without Warburg elements, and three RC elements in parallel. For the spectra in Figures 17 the authors adopted the equivalent circuit model shown in Figure 2 (d). Although these spectra appear to represent but two time constants (i.e., there are two semicircular elements), two are needed to accurately model the depressed higher frequency semicircle, with the third representing the low frequency arc. In this circuit R_s, C_{dl}, and R_{ct} retain their significance in the Randles circuit; C_c represents the capacitance of the inhibitor film, R_{po} is the "pore resistance" of the film; and C_{ox} and R_{ox} are the capacitance and resistance, respectively, of the oxide layer. To improve the fit of model to data, in all cases capacitors were replaced by constant phase elements (CPE) of impedance [6]

$$Z_{CPE} = A_0 (j\omega)^{-\alpha}$$

where α is a constant ($-1 \leq \alpha \leq 1$) and A_0^{-1} corresponds to the capacitance if α is equal to 1. The dependence of the circuit parameters for the coated specimens (excepting R_s, which is not significant) with immersion time is shown in Figures 18 and 19.

Figure 20 (a) shows a Nyquist representation of impedance spectra for a specimen that had been immersed in the brine environment for 8 days prior to treatment with the inhibitor; Figure 20 (b) shows a typical Bode plot for this specimen. The equivalent circuit model of Figure 2 (d) was used to fit these spectra; the corresponding values of the equivalent circuit parameters are exhibited in Figure 21 and 22. The values for the coating capacitance and the double layer capacitance, C_c and C_{dl}, for this "pre-corroded" specimen are larger than those for the as-received aluminum treated with inhibitor, while the capacitance of the oxide film, C_{ox}, is smaller for the specimen treated after initial corrosion. The resistance values for this specimen, Figure 22, as with the other impedance specimens display somewhat more erratic behavior than the capacitance values.

Equivalent circuit in Figure 2 (b) describes the impedance behavior of the inhibitor-coated aluminum substrate. This model is composed of three distinct RC elements, whose correlation with physical features of the system is readily accomplished by examining the magnitudes of the measured capacitance values. The capacitance C_c is of the order of 10^{-10} F/cm^2 and remains essentially constant throughout the experimental period.. We may assume a dielectric constant of 10 for the rather polar species (waxes, alcohols, and free fat acids) comprising wool wax and use, for the parallel plate capacitor constituting the inhibitor film,

$$C = \varepsilon\varepsilon_0/\delta$$

where ε is the dielectric constant of the film, ε_0 is the permittivity of free space

(8.85×10^{-12} farads/meter), and δ is the film thickness. Using the measured capacitance value, the calculated film thickness is of the order of 0.01 cm, in excellent correspondence to the mass of the applied inhibitor film, 9.5 mg cm^{-2}. This film is applied as an aqueous emulsion and air dried and, as the value of C_c remains constant during immersion, the film does not appear to absorb additional water during immersion. The value of C_{ox}, associated with the capacitance of the oxide, ranges from 1.5 to 2×10^{-6} F/cm^{-2}; this corresponds to an oxide film thickness of 4 to 5 nm if a dielectric constant of 9 is assumed. This is just slightly thicker than the thickness of the native Al_2O_3 film, 2 - 4 nm, reported by Scully et al,[14] suggesting that this circuit element is indeed the capacitance of the oxide film and that the rate of growth of the oxide is very slow for inhibitor-coated aluminum. Indeed, in contrast to the untreated alloy the inhibitor-coated specimens did not exhibit visible corrosion during the period of immersion. We associate the capacitance C_{dl} with the double layer, although the value of C_{ox} more closely resembles typical double layer values in aqueous systems. However, the correlation of C_f with the wool wax layer is definitive, and the value of C_{dl} cannot represent the oxide film because the two order of magnitude reduction in thickness implied by the increase in this parameter is not plausible. Rather, we suggest that the value of C_{dl}, increasing from 2×10^{4} F/cm^2 to 0.02 F/cm^2 during the month of immersion, represents the diffusion of electrolyte into the wool wax film to create a very diffuse Gouy layer of charge.

As noted, the values of the resistive elements exhibit a somewhat more erratic behavior than do the capacitance values for these specimens. The oxide resistance, R_{ox}, shows an overall increase which would be associated with growth of aluminum oxide were it not for the invariance of the corresponding capacitance value. An alternative explanation is an increase in the average resistivity of the oxide film through selected closure of film defects. Indeed, such a mechanism would be an explanation for the efficacy of this inhibitor. The resistance of the inhibitor film shows an initial increase but is subsequently constant, suggesting a similar defect closure process. Aside from an

initial order of magnitude increase in value, the charge transfer resistance mimics the shape of the oxide resistance. We believe it plausible that this is not a real effect but an artifact of the modeling process.

CONCLUSION OF MAJOR FINDINGS

- The EIS behavior of aluminum specimens - bare, painted, inhibited, and with crevice geometry - in brackish water is well behaved and suitable for modeling.
- Behavior such as adsorption of water by oxide, paint or inhibitor films is clearly discernible via the EIS technique.
- EIS model parameters are markedly different between damaged and undamaged protective coatings.
- EIS and DC electrode polarization studies confirm the empirically observed benefits of the lanolin-based inhibitors on airframe aluminum alloys.
- The presence of a corroding crevice on the test specimen is readily apparent, both qualitatively (three time constants) and quantitatively ("supercapacitance" behavior, low polarization resistance).

REFERENCES

1. C. I. Chang, in Structure Integrity in Aging Aircraft, C. I. Chang and C. T. Sun eds., ASME AD-Vol. 47, pp. 1-7, ASME Winter Annual Meeting, San Francisco, California, 1995.
2. M. G. Fontana, Corrosion Engineering, McGraw-Hill, New York, 1986.
3. Military Specification Mil-C-0081309D, Corrosion Preventive Compound, Ultra Thin Film, July 1982.
4. Military Specification Mil-C-85054, Corrosion Preventive Compound, Clear, September 1997.
5. B. A. Boukamp, Equivalent Circuit User Manual, 2nd ed., Department of Chemical Technology, University of Twente, The Netherlands, 1989.
6. J. R. Macdonald, Impedance Spectroscopy - Emphasizing Solid Materials and Systems, John Wiley & Sons, New York, 1987.
7. B. E. Conway, "Transition from 'Supercapacitor' to Battery Behavior in Electrochemical Energy Storage", J. Electrochem. Soc. 138, pp. 1539-1548, 1991.
8. I. D. Raistrick, "Electrochemical Capacitors", in Electrochemistry of Semiconductors and Electronics J. McHardy and F. Ludwig eds., Noyes Publications, Park Ridge, New Jersey, 1992.
9. C. Monticelli, F. Zucchi, F. Bonollo, G. Brunoro, A. Frignani and G. Trabanelli, J. Electrochem. Soc. 142, pp. 405-410, 1995.
10. K. S. Yeum and O. F. Devereux, Corrosion 45, pp. 478-487, 1989.

11. O. F. Devereux and K. S. Yeum in ASTM STP 1154, Computer Modeling in Corrosion, R. S. Munn, Ed., pp. 126-142 Philadelphia, 1992.

12. M. Kendig and J. Scully, Corrosion 46, pp. 22-29, 1990.

13. F. Mansfeld, C. Chen F, C. C. Lee and H. Xiao, Corrosion Science 38, pp. 497-513, 1996.

14. J. R. Scully, R. P. Frankenthal, K. J. Hanson, D. J. Siconolfi and J. D. Sinclair, J. Electrochem. Soc. 137, pp.1365-1377, 1990.

Table 1
Equivalent circuit parameters for bare 2024-T3 aluminum.

Immersion time (day)	C_{dl} ($\mu F/cm^2$)	n	R_{ct} (ohm cm^2)	(ohm)	h/D½ ($sec^{½}$)	R_{Do} (ohm cm^2)
1	38.1	0.923	9140	310.6	15.14	4700
3	39.4	0.954	11200	346.0	13.24	4580
5	45.3	0.948	11600	454.5	13.55	6160

Table 2
Equivalent circuit parameters for bare 2024-T3 aluminum in 0.5M NaCl aqueouss solution with pH = 2.

C_{dl} ($\mu F/cm^2$)	n	R_{ct} (ohm cm^2)
154.4	0.885	833

Table 3
Polarization curve parameters for bare 2024-T3 aluminum.

Reaction	s	V^* (mV)	b (mV)	m	i^s (mA)	R (ohm)
1 (C2)	-1	-858.6	39.1	-	-	1.18
2 (C1)	-1	-789.0	97.1	1	0.236	-
3 (A1)	1	-540.3	12.7	-	-	11.29

Table 4
Polarization curve parameters for inhibitor-coated 2024-T3 aluminum.

Reaction	s	V^* (mV)	b (mV)	m	i^s (μA)	R (ohm)
1 (C1)	-1	-1095.47	130.93	1	0.0476	-
2 (A1)	1	-648.4	100.95	1	0.0395	-

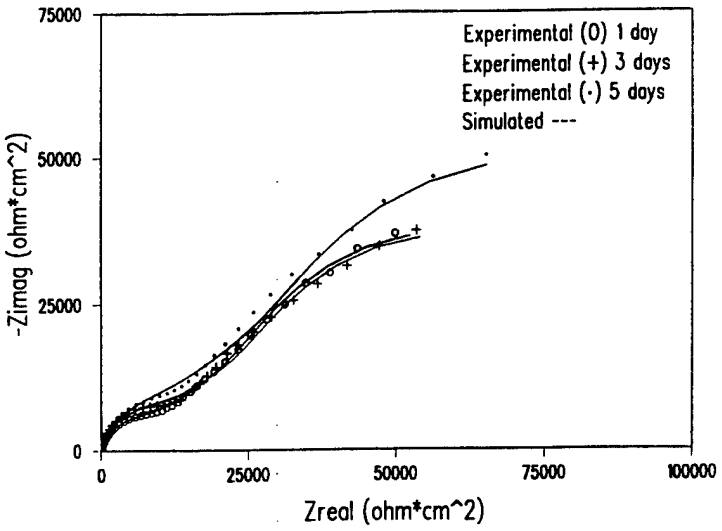

Figure 1 (a). Experimental and model Nyquist plots for bare 2024-T3 aluminum in aqueous 0.5M NaCl solution.

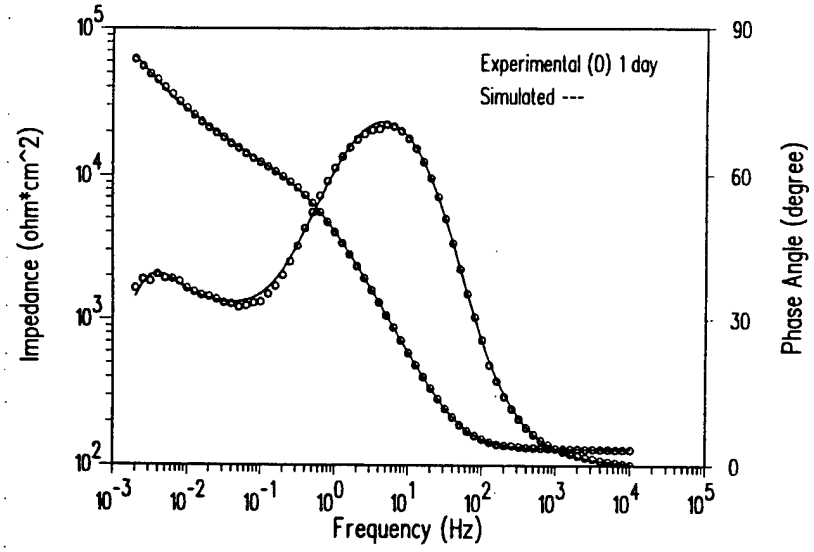

Figure 1 (b). Typical Bode plots corresponding to Figure 1 (a).

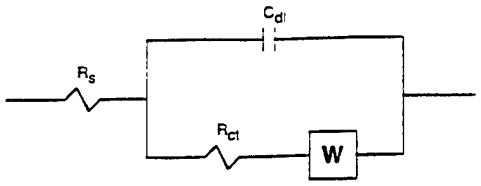

Figure 2 (a). Equivalent electrical circuit for metal without coating.

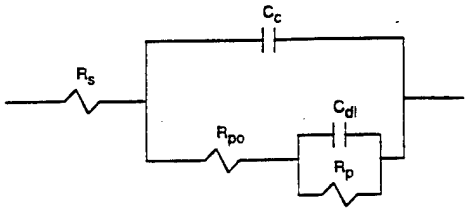

Figure 2 (b). Equivalent electrical circuit for metal with coating.

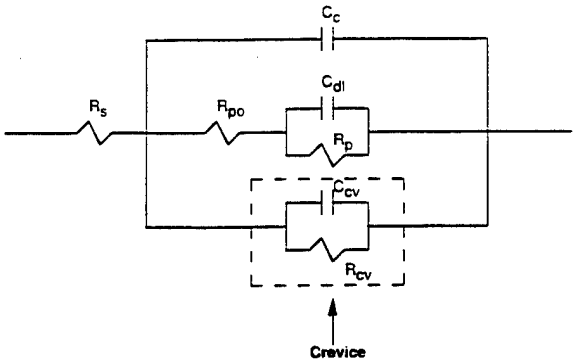

Figure 2 (c). Equivalent electrical circuit for coated metal with simulated joint.

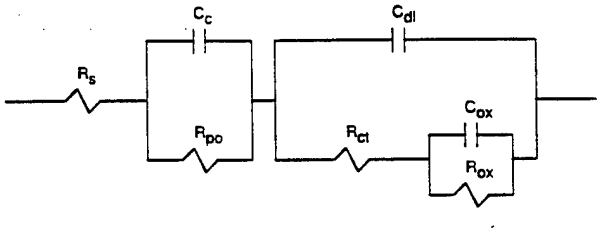

Figure 2 (d). Equivalent electrical circuit for inhibitor-coated metal.

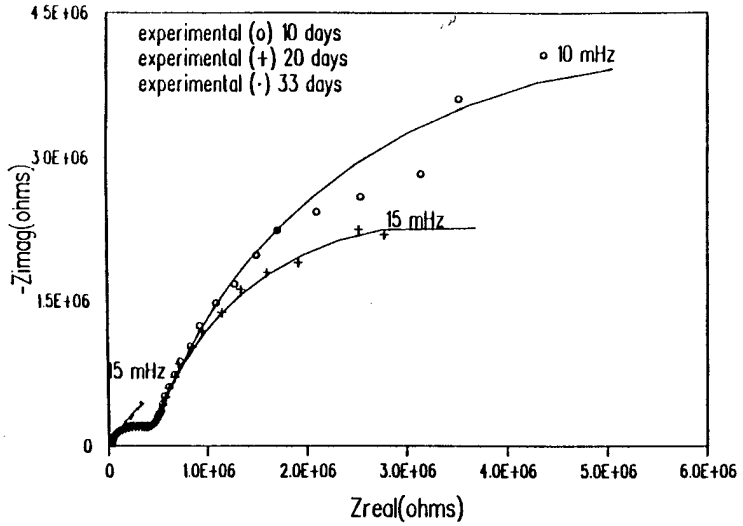

Figure 3 (a). Impedance of painted 2024-T3 aluminum in aqueous 0.5M NaCl solution --- intact paint film.

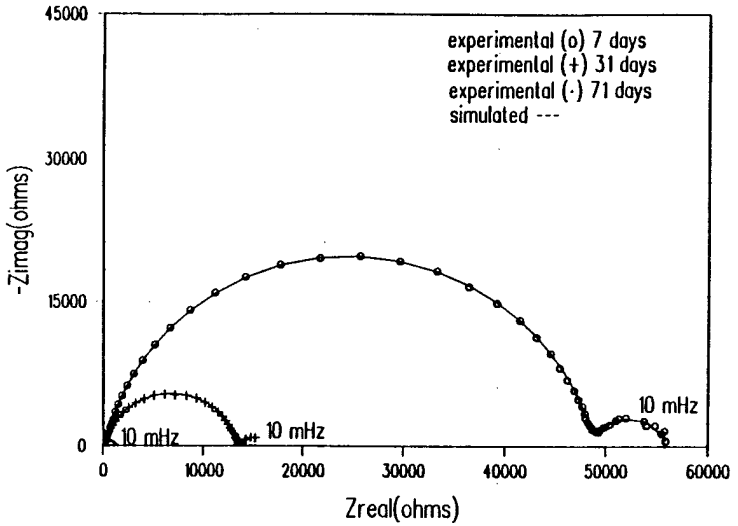

Figure 3 (b). Impedance of painted 2024-T3 aluminum in aqueous 0.5M NaCl solution --- visible blister.

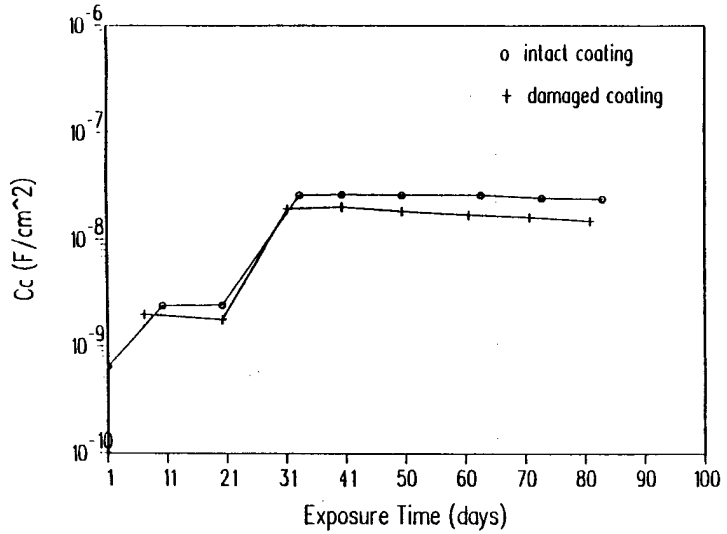

Figure 4. Dependence of coating capacitance (C_c) for intact and damaged coatings on time of immersion in aqueous 0.5M NaCl.

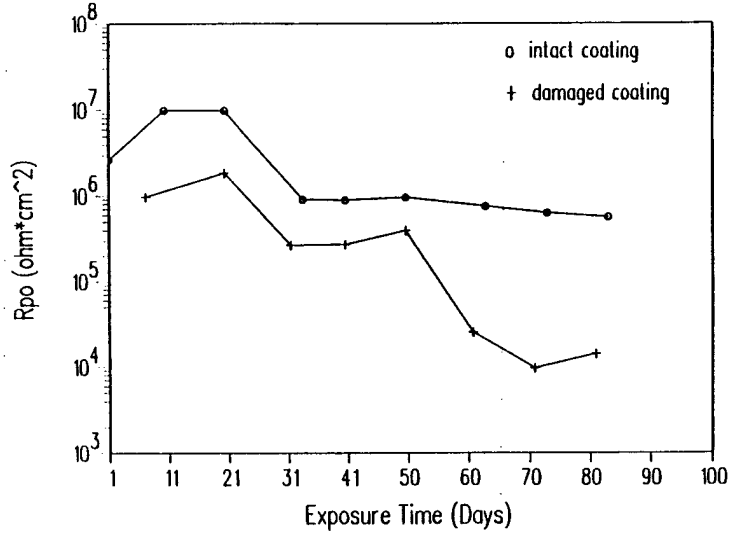

Figure 5. Dependence of pore resistance (R_{po}) for intact and damaged coatings on time of immersion in aqueous 0.5M NaCl.

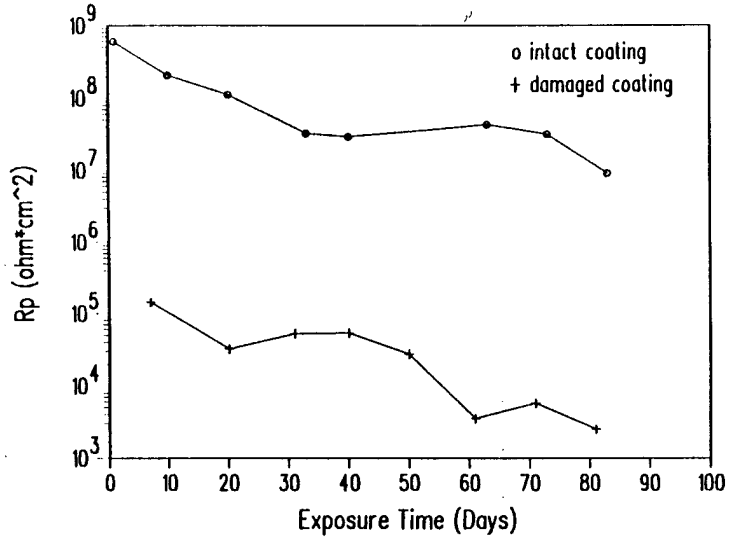

Figure 6. Dependence of polarization resistance (R_p) for intact and damaged coatings on time of immersion in aqueous 0.5M NaCl.

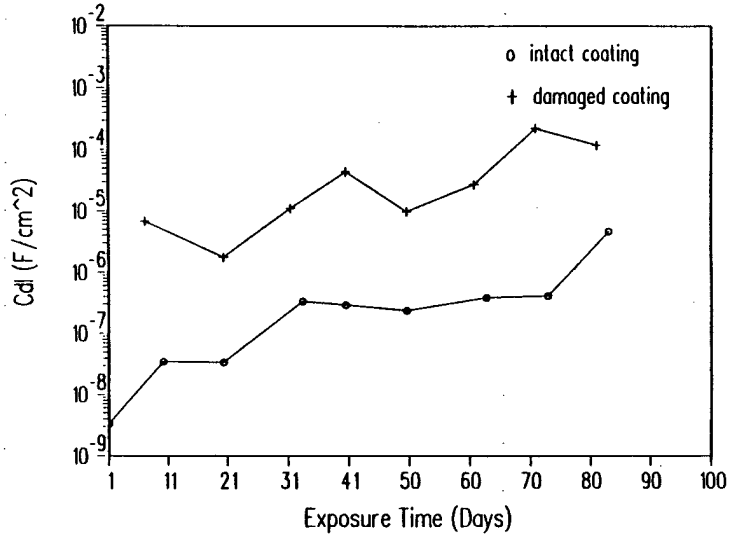

Figure 7. Dependence of double layer capacitance (C_{dl}) for intact and damaged coatings on time of immersion in aqueous 0.5M NaCl.

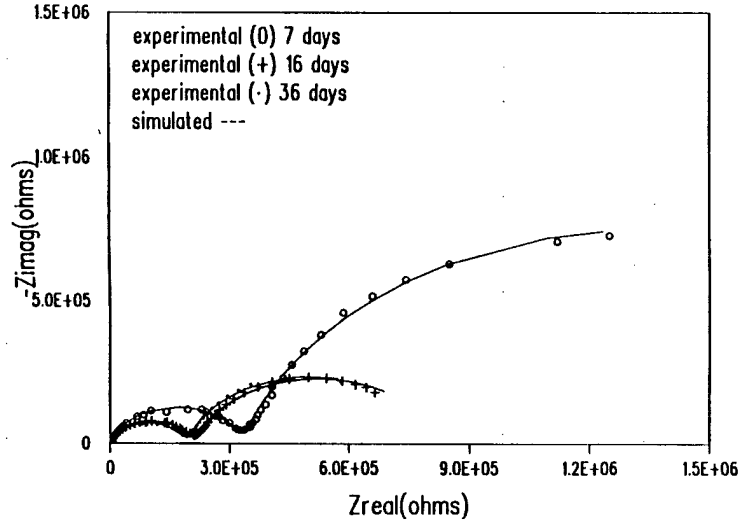

Figure 8 (a). Experimental and model Nyquist plots for coated 2024-T3 aluminum with simulated joint in aqueous 0.5M NaCl solution not showing crevice corrosion.

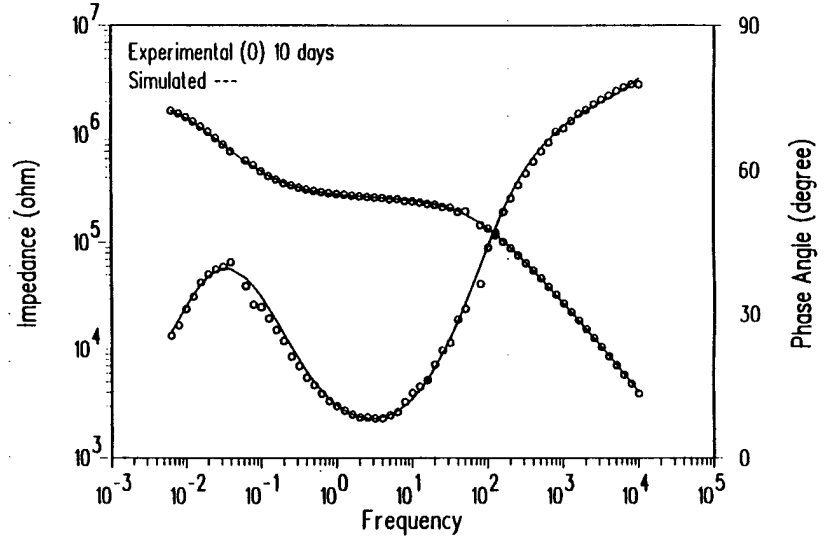

Figure 8 (b). Typical Bode plots corresponding to Figure 8 (a).

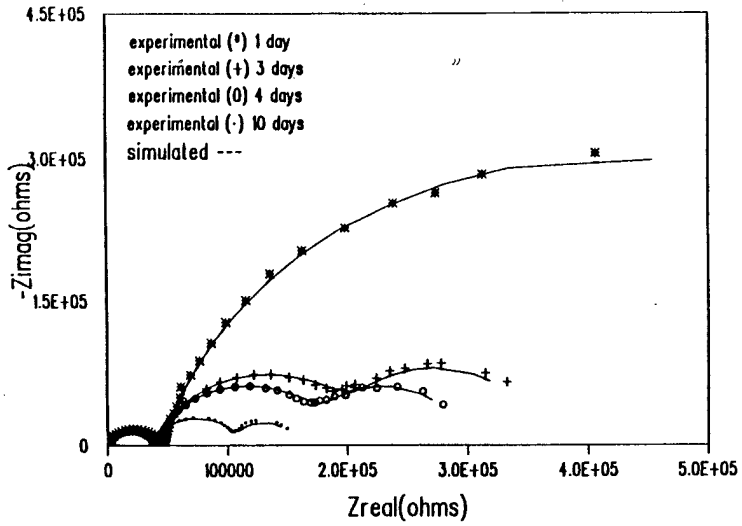

Figure 9 (a). Experimental and model Nyquist plots for coated 2024-T3 aluminum with simulated joint in aqueous 0.5M NaCl solution showing crevice corrosion.

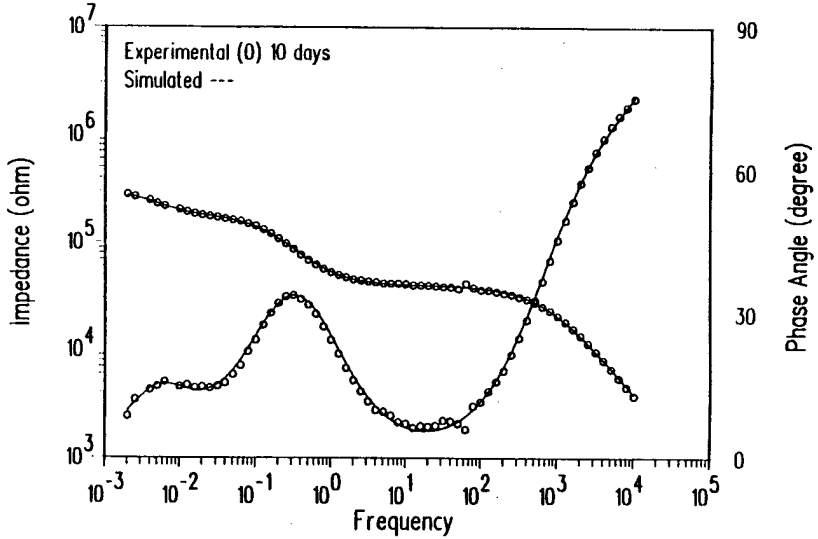

Figure 9 (b). Typical Bode plots corresponding to Figure 9 (a).

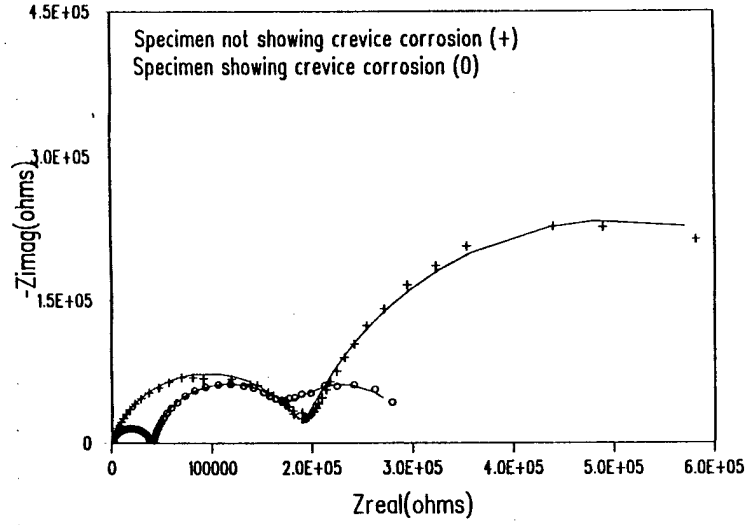

Figure 10. Impedance of coated 2024-T3 aluminum specimens with simulated joint in aqueous 0.5M NaCl solution not showing crevice corrosion (36 days immersion) and showing crevice corrosion (4 days immersion).

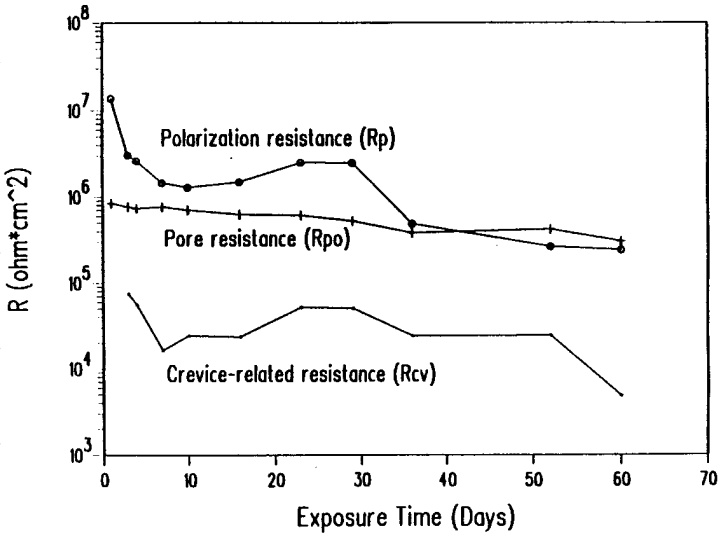

Figure 11. Dependence of resistance for specimen in Figure 9 (a).

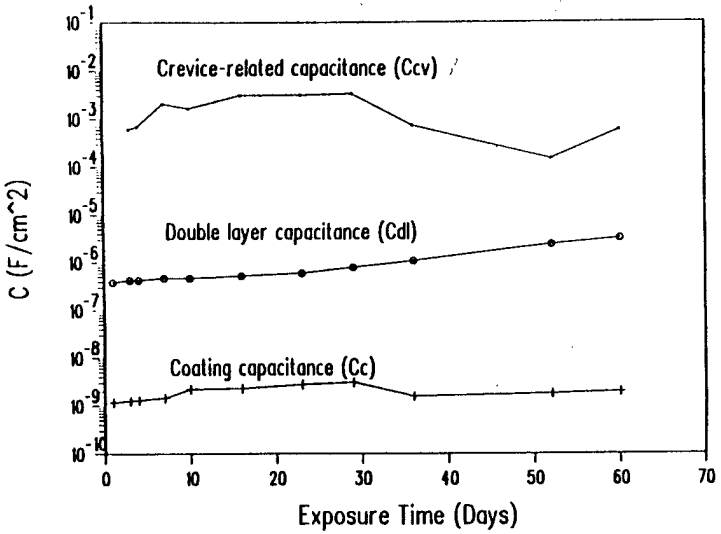

Figure 12. Dependence of capacitance for specimen in Figure 9 (a).

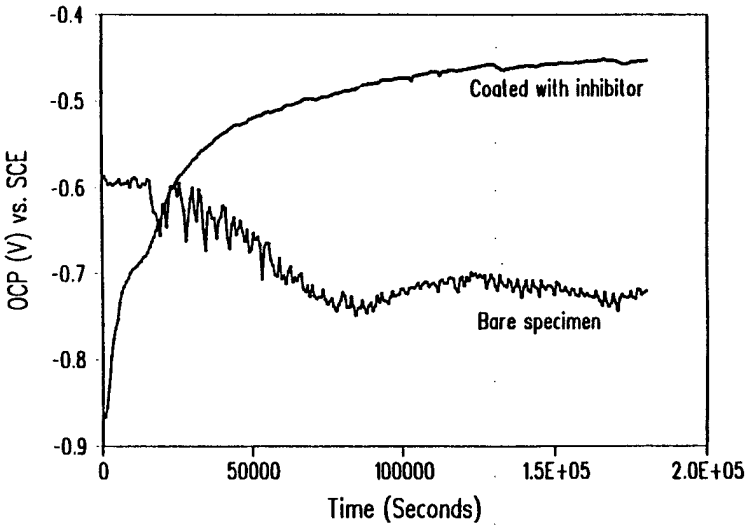

Figure 13. Open circuit potential (OCP) for bare and inhibitor-coated 2024-T3 aluminum vs. immersion time in aqueous 0.5M NaCl.

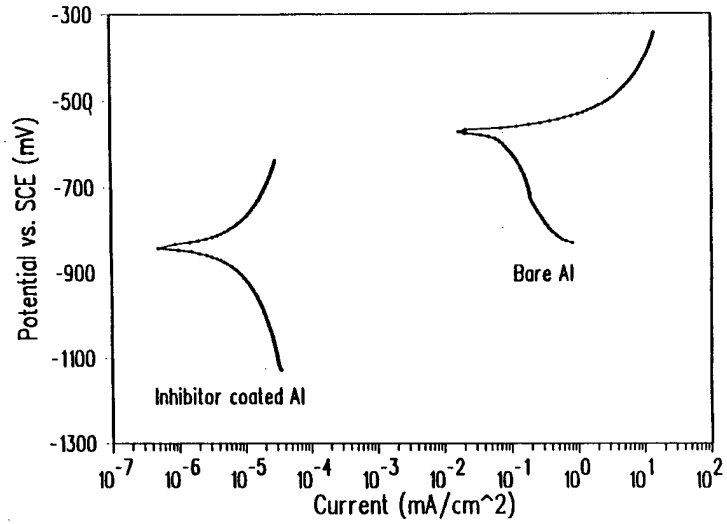

Figure 14. Experimental curves for bare and inhibitor-coated 2024-T3 aluminum in aqueous 0.5M NaCl.

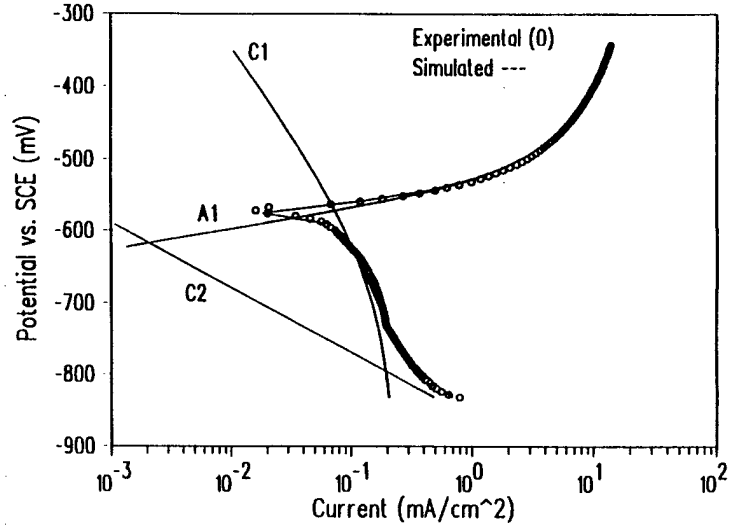

Figure 15. Experimental and model polarization curves, showing individual contributions of electrode reactions, for bare 2024-T3 aluminum in aqueous 0.5M NaCl.

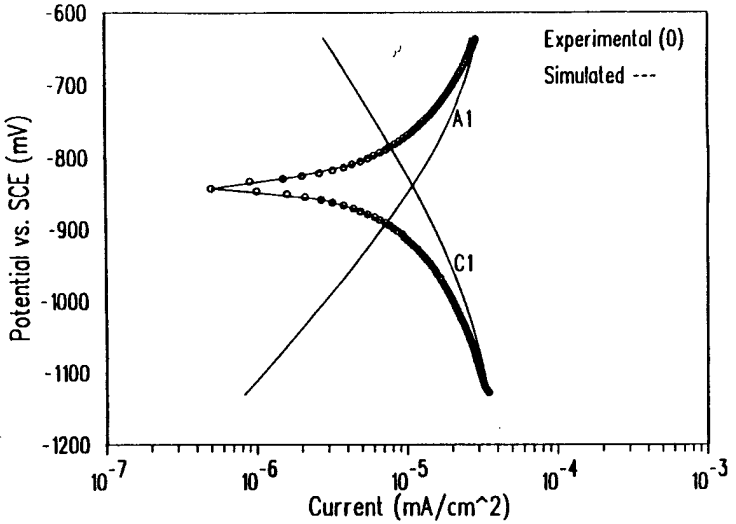

Figure 16. Experimental and model polarization curves, showing individual contributions of electrode reactions, for inhibitor-coated 2024-T3 aluminum in aqueous 0.5M NaCl.

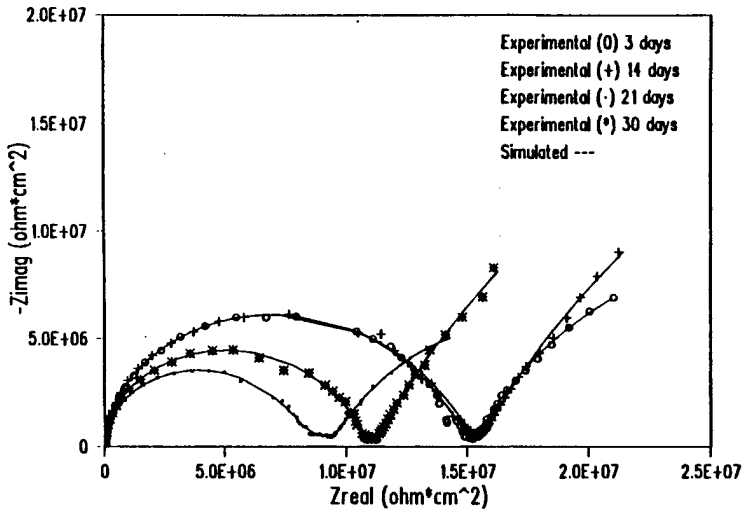

Figure 17 (a). Experimental and model Nyquist plots for inhibitor-coated 2024-T3 aluminum in aqueous 0.5M NaCl.

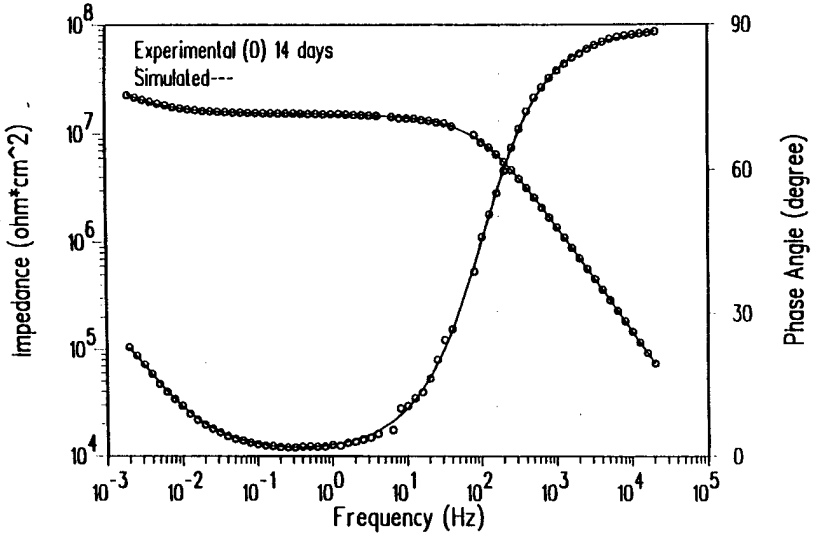

Figure 17 (b). Typical Bode plot corresponding to Figure 17 (a).

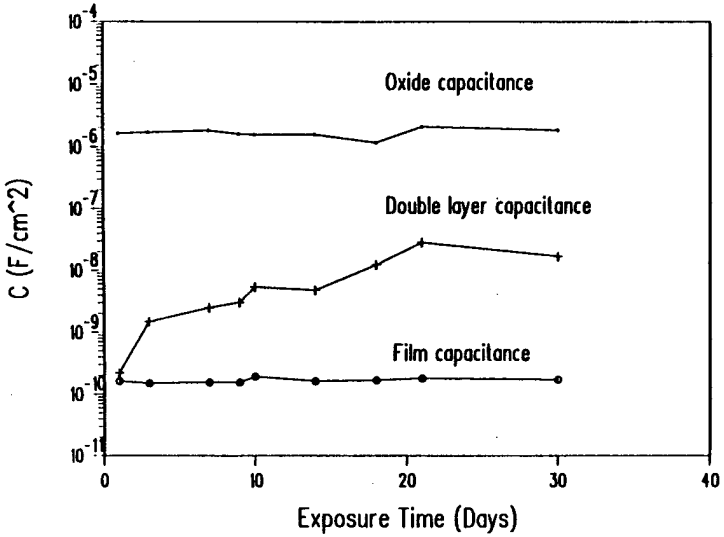

Figure 18. Dependence of capacitance elements for Figure 17 (a) specimen on time of immersion in aqueous 0.5M NaCl.

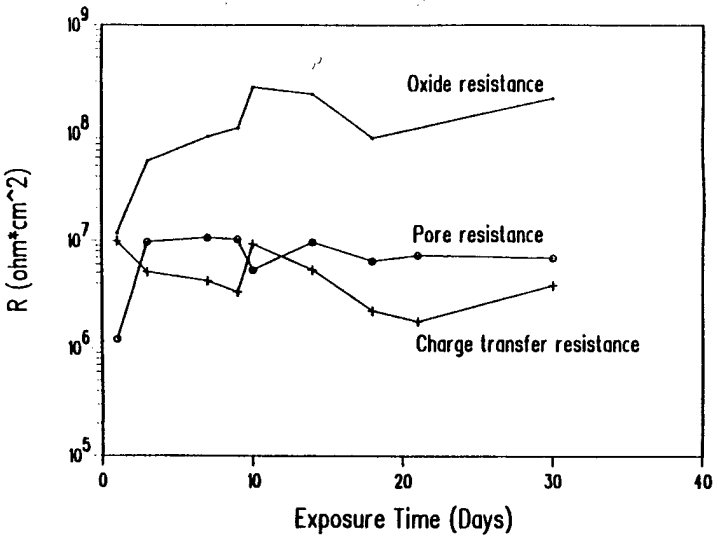

Figure 19. Dependence of resistance elements for Figure 17 (a) specimen on time of immersion in aqueous 0.5M NaCl.

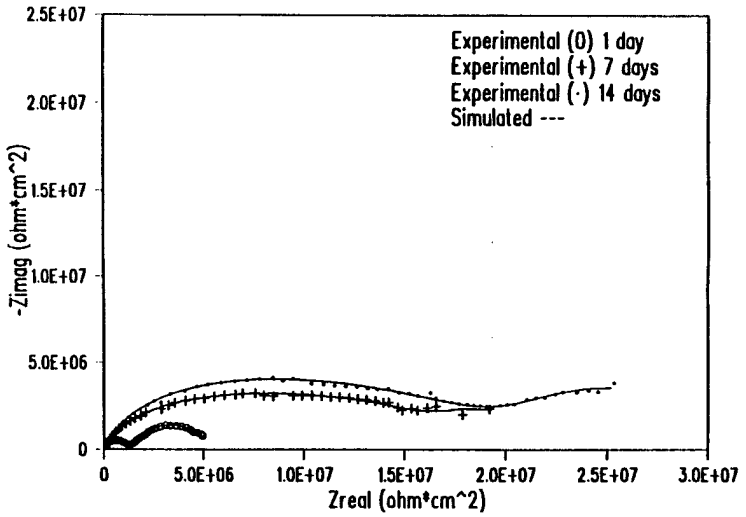

Figure 20 (a). Experimental and model Nyquist plots for 2024-T3 aluminum coated with inhibitor subsequent to 8 days of immersion in aqueous 0.5M NaCl.

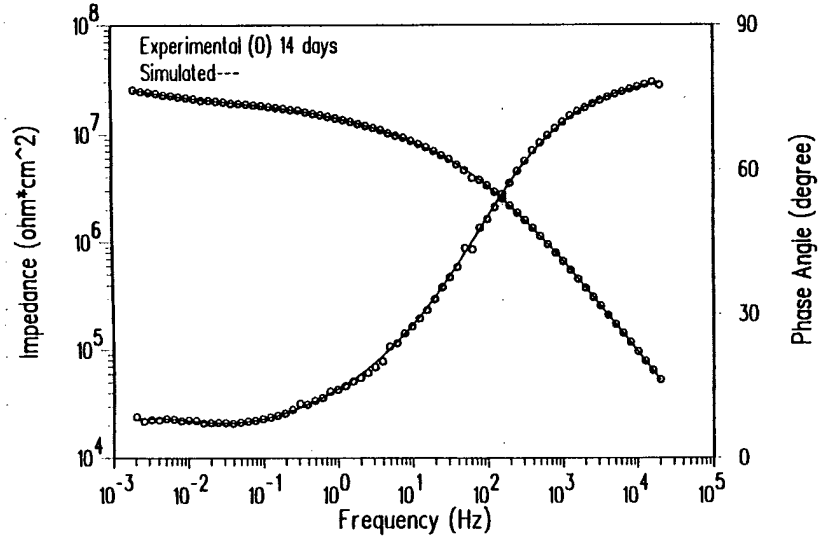

Figure 20 (b). Typical Bode plots corresponding to Figure 20 (a).

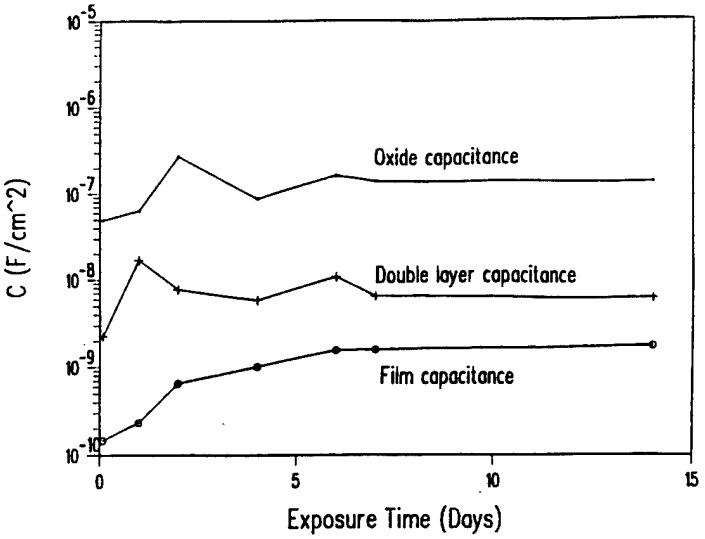

Figure 21. Dependence of capacitance elements for Figure 20 (a) specimen on time of immersion in aqueous 0.5M NaCl after inhibitor application.

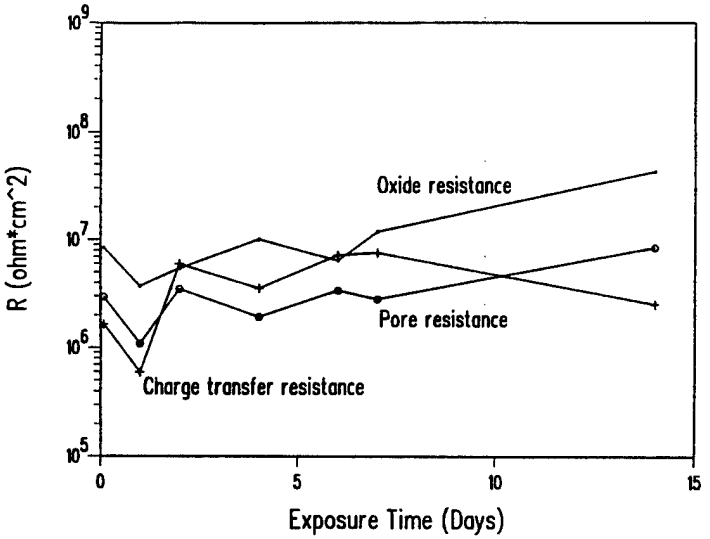

Figure 22. Dependence of resistance elements for Figure 20 (a) specimen on time of immersion in aqueous 0.5M NaCl after inhibitor application.

Part 2

Reconstruction and Wavelet Transforms for Quasilocal Tomography

W. R. Madych *

Abstract

The terms "local" and, more recently, "pseudolocal tomography" have been introduced by several authors and refer to paradigms for recovering high frequency information concerning planar densities f at points x from data which consists of averages of f over lines through x or close to x. The wavelet transform of f is, in some sense, an ideal tool for analyzing local frequency content. In this paper we indicate, among other observations, how reconstruction and wavelet transforms of f can be computed from such data. Furthermore we show how such transforms can be numerically realized via simple modifications of well-established convolution-backprojection algorithms. As part of our development we review the concepts of "local" and "pseudolocal tomography" and show that, in effect, these notions basically involve the computation of a wavelet transform. The results in this paper are based on the observation that Radon's classical inversion formula is a summability formula with an integrable convolution type summability kernel.

1 Introduction

1.1 Background

The values of a sufficiently well behaved scalar valued density or function f defined on the plane, $x \in I\!R^2$, can be recovered from values of its Radon transform via Radon's celebrated classical formula

$$f(x) = -\frac{1}{\pi}\int_0^\infty \frac{dF_x(q)}{q} \tag{1}$$

*Department of Mathematics; University of Connecticut; Storrs, CT 06269-3009. Partially supported by AFOSR Grant F49620-93-1-0565

where $F_x(q)$ is the average of all the integrals of f over lines which are distance q from x. For example[1] see [29, page 245] also [4, Appendix A], [8], [22], and [25].

It is well known that formula (1) contains features which make it difficult to use in practical applications. Among these are (i) the fact that the integral in the formula is not proper and (ii) the fact that the inversion is not local, namely, the evaluation of $f(x)$ requires the integrals of f over all lines, not only those through x or close to x.

Over the years many publications have dealt with (i), for example see [4], [10], or [22] for detailed expositions and extensive bibliographies. Relatively recently several publications have addressed (ii), see [6, 7, 30, 12]. The basic idea is to use the integrals of f over lines close to x not to recover the value $f(x)$ but to obtain certain high frequency content of f near x.

A currently fashionable tool for analyzing the frequency content of signals or functions is the so-called wavelet transform. For a sufficiently well behaved scalar valued function f defined on the plane, $\mathbb{R}^2$, its wavelet transform is a one parameter family $W_\Psi f(a,x)$, $a>0$, of functions defined by the formula

$$W_\Psi f(a,x) = \frac{1}{a^2}\int_{\mathbb{R}^2} \Psi(y/a) f(x-y)dy \tag{2}$$

where Ψ is an integrable, usually radial, function with mean value 0. The function Ψ is sometimes referred to as the analyzing wavelet[2]. The effectiveness of the wavelet transform in practical applications is well known, for example see [3].

Since any nice radial function Ψ enjoys a convenient representation as a uniform sum of ridge functions, see [20], the corresponding wavelet transform of f can be computed directly from the values of the Radon transform of f via a formula involving convolution and backprojection[3]. Such formulas, unlike (1), involve proper integrals nevertheless, like (1), these formulas are generally not local. One of the objectives of this article is to show how such formulas can be localized.

[1]The Radon transform and its inversion is discussed in more detail in Subsection 2.1. A reproduction of Radon's original paper [25] is in [8] and its English translation is in [4]. A contemporary derivation of this formula together with an outline of Radon's proof of its validity can be found in [22].

[2]Note that the transform depends on the analyzing wavelet Ψ. A popular choice is the Laplacian of the Gaussian or the so-called "Mexican hat"

$$\Psi(x) = (|x|^2 - 2)e^{-|x|^2}$$

but, of course, many other choices are possible. The normalizing factor preceding the integral may involve a different power of a depending on the usage and the authors' tastes. This definition and some of its consequences are discussed in more detail in Subsection 2.5

[3]This is explained in more detail in Section 2.5

1.2 Overview

We consider the natural approximations

$$g_\epsilon f(x) = -\frac{1}{\pi}\int_\epsilon^\infty \frac{dF_x(q)}{q} \tag{3}$$

of (1) parametrized by positive ϵ and observe that

$$g_\epsilon f(x) = \epsilon^{-2}\int_{\boldsymbol{R}^2} k(y/\epsilon) f(x-y)dy \tag{4}$$

where k is a positive radial function with

$$\int_{\boldsymbol{R}^2} k(x)dx = 1\,.$$

Identity (4) means that $g_\epsilon f(x)$ is, in effect, the convolution of f with an approximation of the identity kernel of "thickness" ϵ. This routinely implies that $\lim_{\epsilon\to 0} g_\epsilon f(x) = f(x)$ for suitably well behaved f and, incidentally, provides an alternate proof of (1).

Formulas like[4] (3) and (4) are the basis of our "transforms for quasilocal tomography". Namely, $\Psi(x) = 2k(2x) - k(x)$ has mean value 0 and the corresponding wavelet transform can be computed via

$$W_\Psi f(a,x) = -\frac{1}{\pi}\int_{a/2}^a \frac{dF_x(q)}{q}\,. \tag{5}$$

In other words, the value of the wavelet transform $W_\Psi f(a,x)$ can be computed using only the integrals of f over lines which intersect the disc of radius a. Furthermore, for any positive ϵ,

$$\sum_{j=-\infty}^{\infty} W_\Psi f(2^j\epsilon, x) = f(x) \tag{6}$$

and, since for sufficiently large j the terms $Wf(2^j\epsilon, x)$ contain low frequency information which can often be ignored, formula (6) can be used as the basis of a "quasilocal" approximate inversion formula.

The inversion method suggested by (5) and (6) is potentially of some practical significance. For instance, we show how, in one particular realization, (5) can be approximately evaluated using parallel beam X-ray data and a slightly modified version of the classical backprojection algorithm introduced by Shepp and Logan [28].

In our development we include the following:

- a brief review of some elementary facts concerning the Radon transform and its inversion;

[4]We use slightly different variants of the inversion formula in our development.

- a recollection of the notions of "local tomography" and "pseudolocal tomography" as found in [6, 7, 30] and [12] respectively and an indication of a connection between the two notions;

- a derivation of relationships like those implied by the pairs of equations (3), (4) and (5), (6) and an indication of some of the consequences of these formulas;

- a brief review of the definition and the motivation of the wavelet transforms, a general paradigm for computing such transforms in terms of Radon transform data, and an indication of the fact that, in effect, "local" and "pseudolocal tomography" involve the computation of a wavelet transform;

- discrete analogues of formulas like (5) and (6) which lead to various reconstruction algorithms;

- numerical examples illustrating potential applications of these algorithms.

1.3 Remarks, conventions, and acknowledgements

The Radon transform and the notions of wavelets or wavelet transform have been recently treated together in many articles, for example see [1, 5, 11, 26]. However, to my knowledge, this is the first time that certain basic relationships such as those expressed by the pairs of equations (3), (4) and (5), (6) have been recorded.

Most of the development can be found in Section **2** where, to maintain readability, certain technical details and other pertinent, but not essential, remarks are kept to a minimum. The main development is contained in Subsections **2.1**, **2.3**, **2.5**, and **2.7**. Subsections **2.2**, **2.4**, and **2.6** contain material on "local" and "pseudolocal tomography" and are not critical to this development; they are included to bring attention to the natural connection between these notions and wavelet transforms. Discrete analogues of some of the formulas found in **2.3** and **2.7** are indicated in Subsection **2.8**. Such analogues can be used as the basis for algorithms for the reconstruction of $f(x)$ and its wavelet transform from its Radon transform data; this is illustrated by the numerical examples in Subsection **2.9**.

Subsection **3.n** is devoted to the details and remarks omitted in Subsection **2.n**.

We use standard terminology, notation, and conventions. Here we simply remind the reader of the following:

- The convolution $f * g$ of two scalar valued functions f and g on $\mathbb{R}^2$ (or $\mathbb{R}$) is defined by

$$f * g(x) = \int f(y)g(x-y)dy$$

where the integral is taken over all of $\mathbb{R}^2$ (or $\mathbb{R}$) whenever the integral is well defined and distributionally otherwise.

- The Fourier transform $\hat{f}$ of a function f on $\mathbb{R}^2$ (or $\mathbb{R}$) is defined by

$$\hat{f}(\xi) = \int e^{-i\langle \xi, x\rangle} f(x)dx$$

where the integral is taken over all of $\mathbb{R}^2$ (or $\mathbb{R}$) whenever the integral is well defined and distributionally otherwise. $\langle \xi, x\rangle$ denotes the usual scalar product of ξ and x.

- Whether the convolution or Fourier transform is to be interpreted in the bivariate or univariate sense should be clear from the context.

- Generic constants, whose meaning should be clear from the context, are denoted by c.

In what follows f always denotes an integrable scalar valued function on the plane $\mathbb{R}^2$, that is, $\int_{\mathbb{R}^2} |f(x)|dx$ is finite. Other restrictions on f will be given as needed.

This work was partially motivated by the appearance of [12] which was brought to my attention by Dr. Arje Nachman of the AFOSR.

2 Development

2.1 The Radon transform and an inverse

Recall that the Radon transform $Rf(\theta, t)$, $0 \le \theta < 2\pi$, $-\infty < t < \infty$, of an integrable function f on $\mathbb{R}^2$ may be defined by

$$Rf(\theta, t) = \int_{-\infty}^{\infty} f(tu_\theta + sv_\theta)ds$$

where $u_\theta = (\cos\theta, \sin\theta)$ and $v_\theta = (-\sin\theta, \cos\theta)$. Since it is often convenient to view $Rf(\theta, t)$ as a family of functions of t parametrized by θ we use the abbreviated notation

$$f_\theta(t) = Rf(\theta, t)\ .$$

The precise version of Radon's inversion formula is

$$f(x) = \frac{1}{\pi} \lim_{\epsilon \to \infty} \left\{ \frac{F_x(\epsilon)}{\epsilon} - \int_\epsilon^\infty \frac{F_x(t)}{t^2} dt \right\} \tag{7}$$

where

$$F_x(t) = \frac{1}{2\pi}\int_0^{2\pi} f_\theta(\langle x, u_\theta\rangle + t)d\theta\,,$$

see [25, formula III']. Radon showed the validity of this formula under the assumption that f is continuous and satisfies two other technical conditions. Under these conditions integration by parts shows the equivalence of (1) and (7).

In Subsection **2.3** we show that (7) remains valid under more general conditions.

2.2 Local tomography: low and high band pass filters

Note that in order to determine $f(x)$ via (7) knowledge of $f_\theta(t)$ for all t and θ is required. On the other hand applying the formal adjoint $R^\#$ of R to $f_\theta(t)$ results in

$$R^\# Rf(x) = \int_0^{2\pi} f_\theta(\langle x, u_\theta\rangle)d\theta\,. \tag{8}$$

Observe that the above formula for $R^\# Rf(x)$ in terms of $f_\theta(t)$ is very local in the sense that only integrals of f over lines through x are used to compute $R^\# Rf(x)$. The relationship between $R^\# Rf$ and f may be more transparent from

$$R^\# Rf(x) = 4\pi J * f(x)$$

where

$$J(x) = \frac{1}{2\pi|x|}\,.$$

Since the Fourier transform of $J * f$ is

$$\widehat{J*f}(\xi) = |\xi|^{-1}\hat{f}(\xi)\,,$$

$R^\# Rf$ may be regarded as a low band pass filtered version of f.

If f is sufficiently well behaved and the Laplacian Δ is applied to both sides of (8) then interchanging the order of integration and differentiation on the right hand side results in

$$\Delta R^\# Rf(x) = \int_0^{2\pi} f''_\theta(\langle x, u_\theta\rangle)d\theta\,, \tag{9}$$

where $f''_\theta(t)$ is the second derivative of $f_\theta(t)$ with respect to t. Note that formula (9) for $\Delta R^\# Rf(x)$ in terms of $f_\theta(t)$ is only slightly less local than (8) in the sense that only integrals of f over all lines which pass through an arbitrarily small neighborhood of x are needed to compute $\Delta R^\# Rf(x)$.

Using Λ to denote the transformation defined by

$$\Lambda f(x) = -\Delta J * f(x)$$

we see that it may also be expressed as

$$\Lambda f(x) = \frac{-1}{4\pi}\Delta R^{\#} Rf(x)$$

and computed via (9). Note that mapping $f \to J*f$ is the inverse of Λ since $J*\Lambda f = f$, in other words

$$\Lambda^{-1} f(x) = J*f(x)\,.$$

Since the Fourier transform of Λf is

$$\widehat{\Lambda f}(\xi) = |\xi|\hat{f}(\xi)\,,$$

Λf may be regarded as a high band pass filtered version of f. Thus one may obtain both low and high band pass versions of f, $\Lambda^{-1} f = \frac{1}{4\pi} R^{\#} Rf$ and $\Lambda f = \frac{-1}{4\pi}\Delta R^{\#} Rf$, from local Radon transform data via formulas (8) and (9). Both versions can be used to obtain information on f from its Radon transform data. For example, in [6, 7, 30] the authors suggest the reconstruction of linear combinations of Λf and $\Lambda^{-1} f$ rather than the density function f itself; they refer to this as "lambda" or "local tomography".

2.3 Low band pass filters and inversion formulas

Consider the natural approximation $g_\epsilon f$ of (7) parametrized by ϵ and defined by

$$g_\epsilon f(x) = \frac{1}{\pi}\left\{\frac{F_x(\epsilon)}{\epsilon} - \int_\epsilon^\infty \frac{F_x(t)}{t^2}dt\right\} \tag{10}$$

The fact that the transformation $f \to g_\epsilon f$ is translation invariant implies that $g_\epsilon f$ is the convolution of f with some distribution. Appropriate calculations show that

$$g_\epsilon f(x) = k_\epsilon * f(x) \tag{11}$$

where

$$k_\epsilon(x) = \epsilon^{-2} k\left(x/\epsilon\right)\,,$$

$$k(x) = \frac{1}{\pi^2 |x|^2 \sqrt{|x|^2 - 1}}\chi(|x|)\,,$$

and

$$\chi(t) = \begin{cases} 0 & \text{if} \quad |t| \le 1 \\ 1 & \text{if} \quad |t| > 1\,. \end{cases}$$

Note that k enjoys the following properties:

i. k is a non-negative radial function on $\mathbb{R}^2$.

ii. $\int_{\mathbb{R}^2} k(x)dx = 1\,.$

iii. $\int_{R^2} |x|^\alpha k(x)dx$ is finite for $0 < \alpha < 1$.

iv. $|x|k(x) \leq c|x|^{-2}$ for $|x| > 2$.

Thus g_ϵ is simply the convolution of f with a radial summability kernel, or approximation of the identity, of "thickness" ϵ. Indeed formula (11) routinely implies (7) whenever f is continuous. For other standard consequences of identity (11) see the Theorem below.

Use of the representation[5]

$$(12) \quad f(x) = \frac{-1}{8\pi^2} \int_0^{2\pi} \int_{-\infty}^{\infty} \frac{f_\theta(\langle x,u_\theta\rangle + t) - 2f_\theta(\langle x,u_\theta\rangle) + f_\theta(\langle x,u_\theta\rangle - t)}{t^2} dt d\theta$$

together with the approximation suggested by (10) results in a similar conclusion with a different summability kernel. To wit, consider the approximation $G_\epsilon f$ of (12) defined by

$$(13)\ G_\epsilon f(x) = \frac{-1}{8\pi^2} \int_0^{2\pi} \int_{|t|>\epsilon} \frac{f_\theta(\langle x,u_\theta\rangle + t) - 2f_\theta(\langle x,u_\theta\rangle) + f_\theta(\langle x,u_\theta\rangle - t)}{t^2} dt d\theta$$

then the analogous manipulations which gave (11) from (10) result in

$$(14) \qquad G_\epsilon f(x) = K_\epsilon * f(x)$$

where

$$K_\epsilon(x) = \epsilon^{-2} K\left(x/\epsilon\right) ,$$

$$K(x) = \frac{1}{\pi^2} \left\{ \frac{1}{|x|} - \frac{\sqrt{|x|^2 - 1}}{|x|^2} \chi(|x|) \right\}$$

and χ is the indicator function of $\{t : |t| > 1\}$ as above. The kernel K may be re-expressed as

$$K(x) = \frac{1}{\pi^2} \left\{ \frac{1}{|x|} \{1 - \chi(|x|)\} + \frac{1}{|x|^2 \left\{ |x| + \sqrt{|x|^2 - 1} \right\}} \chi(|x|) \right\}$$

to see that it is an integrable radial function which is decreasing as a function of $|x|$ and $K(x) = O(|x|^{-3})$ as $|x|$ tends to ∞.

Note that K enjoys properties **i-iv** enjoyed by k above. Thus $G_\epsilon f$, like $g_\epsilon f$, is the convolution of f with a radial summability kernel of thickness ϵ. Because K is dominated by an integrable radially decreasing function, namely itself, it is significantly better than k which does not enjoy this property. Relationship (14) together with the properties of K routinely imply various results concerning the convergence of $G_\epsilon f(x)$ to $f(x)$ as ϵ goes to 0. For example:

[5]This inversion formula can be found in [20] on page 196. See also Subsection **3.3**.

Theorem

i $\lim_{\epsilon \to 0} G_\epsilon f(x) = f(x)$ almost everywhere.

ii $\lim_{\epsilon \to 0} \|f - G_\epsilon f\|_{L^1} = 0\,.$

iii If f is in L^p for some p, $1 < p < \infty$, then $\lim_{\epsilon \to 0} \|f - G_\epsilon f\|_{L^p} = 0\,.$

iv If f is in L^∞ and continuous at x then

$$\lim_{\epsilon \to 0} G_\epsilon f(x) = f(x).$$

Furthermore, if f is uniformly continuous then this holds uniformly in x.

v If f is L^∞ and Hölder continuous[6] at x of order α for some positive α then

$$|f(x) - G_\epsilon f(x)| \le c \begin{cases} \epsilon^\alpha & \text{if} \quad 0 < \alpha < 1, \\ \epsilon\{1 + |\log \epsilon|\} & \text{if} \quad \alpha = 1, \\ \epsilon & \text{if} \quad \alpha > 1 \end{cases} \tag{15}$$

where c is independent of ϵ. Furthermore, if f is uniformly Hölder continuous on $\mathbb{R}^2$ then this estimate is valid for all x with a constant c independent of ϵ and x.

vi Suppose Γ is an analytic arc, $x \in \Gamma$ and B is an open neighborhood of x such that the complement of $\Gamma \bigcap B$ in B has two components B_1 and B_2. If the restrictions of f to B_1 and B_2 have extensions to the closures of B_1 and B_2 respectively which are uniformly Hölder continuous of order α for some positive α then (15) holds with the left hand side of the inequality replaced with

$$\left| \frac{1}{2} \left\{ \lim_{y \to x \text{ and } y \in B_1} f(y) + \lim_{y \to x \text{ and } y \in B_2} f(y) \right\} - G_\epsilon f(x) \right| .$$

[6]The function f is said to be Hölder continuous of order α at x if the k-th order difference of f in y at x is dominated by a constant times $|y|^\alpha$, where k is the least integer greater than α. Thus, if α is in the range $0 < \alpha < 1$, this means that

$$|f(x+y) - f(x)| \le C|y|^\alpha\,,$$

where C is a constant independent of y; if α is in the range $1 \le \alpha < 2$, this means that

$$|f(x+y) - 2f(x) + f(x-y)| \le C|y|^\alpha\,,$$

etc. The function f is said to be uniformly Hölder continuous of order α if it is Hölder continuous of order α at every point x and the constant C is also independent of x. Note that if f is differentiable then it is Hölder continuous of order one, if f is twice differentiable then it is Hölder continuous of order two, etc.

vii If f is in L^p for some p, $2 < p \leq \infty$, then $G_\epsilon f$ is Hölder continuous of order $1 - 2/p$. If f is Hölder continuous of order α then $G_\epsilon f$ is Hölder continuous of order $\alpha + 1$.

Items **ii** - **vii** remain valid if $G_\epsilon f$ is replaced with $g_\epsilon f$. See Subsection **3.3** for more details. Similar results are valid for regularized variants of $G_\epsilon f$ and $g_\epsilon f$.

Note that the Fourier transform of G_ϵ is given by

$$\widehat{G_\epsilon f}(\xi) = \widehat{K}(\epsilon\xi)\hat{f}(\xi)\,.$$

Since $\widehat{K}$ is continuous, $\widehat{K}(0) = 1$, and $\lim_{|\xi|\to\infty} \widehat{K}(\xi) = 0$, G_ϵ is the result of processing f through a low frequency band pass filter which converges to the identity as ϵ tends to 0. Similar remarks are valid concerning $g_\epsilon f$ with $\hat{k}(\epsilon\xi)$ playing the role of the low band pass filter $\widehat{K}(\epsilon\xi)$.

2.4 Local or pseudolocal tomography

For sufficiently well behaved f the inversion formula (1) can be re-expressed as

$$f(x) = \frac{1}{4\pi^2}\int_0^{2\pi}\int_{-\infty}^{\infty} \frac{f'_\theta(\langle x, u_\theta\rangle - t)}{t} dt d\theta \tag{16}$$

where $f'_\theta(t)$ is the derivative of $f_\theta(t)$ with respect to t. In view of this expression the authors of [12] consider the decomposition

$$f(x) = h_\epsilon f(x) + \{f(x) - h_\epsilon f(x)\} \tag{17}$$

where

$$h_\epsilon f(x) = \frac{1}{4\pi^2}\int_0^{2\pi}\int_{-\epsilon}^{\epsilon} \frac{f'_\theta(\langle x, u_\theta\rangle - t)}{t} dt d\theta\,. \tag{18}$$

and suggest the reconstruction of the quantity $h_\epsilon f$ rather than the density function f itself to obtain high frequency information concerning f. They refer to this as "pseudolocal tomography".

Note that (17) may be expressed as

$$f(x) = h_\epsilon f(x) + g_\epsilon f(x)$$

where

$$h_\epsilon f(x) = f(x) - g_\epsilon f(x) \tag{19}$$

and $g_\epsilon f$ is defined by (10). The last relation implies that the Fourier transform of $h_\epsilon f$ may be expressed as

$$\widehat{h_\epsilon f}(\xi) = \{1 - \hat{k}(\epsilon\xi)\}\hat{f}(\xi)$$

where, as indicated in the previous subsection, $\hat{k}(\epsilon\xi)$ is a low frequency band pass filter. Thus $h_\epsilon f$ may be regarded as the result of processing f through a high frequency band pass filter which converges to 0 as ϵ tends to 0.

A decomposition analogous to (17) can be made using representation (12). Namely

$$f(x) = H_\epsilon f(x) + G_\epsilon f(x)$$

where

$$H_\epsilon f(x) = f(x) - G_\epsilon f(x)$$

and $G_\epsilon f$ is defined by (13). In this case, for sufficiently well behaved f, the formula for $H_\epsilon f(x)$ may be expressed as

$$(20)\quad H_\epsilon f(x) = \frac{-1}{8\pi^2}\int_0^{2\pi}\int_{-\epsilon}^{\epsilon} \frac{f_\theta(\langle x,u_\theta\rangle+t)-2f_\theta(\langle x,u_\theta\rangle)+f_\theta(\langle x,u_\theta\rangle-t)}{t^2}dtd\theta\,.$$

It should be clear that $H_\epsilon f$ may also be regarded as the result of processing f through a high frequency band pass filter which converges to the 0 as ϵ tends to 0.

It is important to note that, by virtue of (18) and (20), both $h_\epsilon f(x)$ and $H_\epsilon f(x)$ are, in principle, computable[7] in terms of integrals of f over lines which intersect the disk of radius ϵ centered at x. For this reason they may be regarded as being computable from local Radon transform data of f.

Thus "local tomography" whose objective is to compute Λf and "pseudolocal tomography" whose objective is to compute $h_\epsilon f$ appear to take different routes to roughly the same goal. However, the fact that both Λf and $h_\epsilon f$ are high frequency band filtered versions of f which can be computed in terms of local Radon transform data is not the only similarity between these functions. Observe that the integrand in (18) may be replaced by

$$\frac{f'_\theta(\langle x,u_\theta\rangle - t) - f'_\theta(\langle x,u_\theta\rangle)}{t}$$

which in turn is well approximated by $-f''_\theta(\langle x,u_\theta\rangle)$ if ϵ is sufficiently small. Thus for sufficiently small ϵ we may write

$$h_\epsilon f(x) \approx \frac{-\epsilon}{4\pi^2}\int_0^{2\pi} f''_\theta(\langle x,u_\theta\rangle)d\theta = \frac{\epsilon}{\pi}\Lambda f(x)$$

or, more precisely, for sufficiently well behaved f

$$(21)\qquad h_\epsilon f(x) = \frac{\epsilon}{\pi}\Lambda f(x) + o(\epsilon) \quad \text{as } \epsilon \to 0.$$

Further connections are discussed in Subsection **2.6**.

[7]These formulas are valid if f is sufficiently smooth. Otherwise one should use "regularized" analogues, see Subsection **2.6**.

2.5 Wavelet transforms and tomography

Recall that the wavelet transform of f via the "wavelet" Ψ is defined by

$$W_\Psi f(a,x) = \Psi_a * f(x)$$

where $a > 0$, $\Psi_a(x) = a^{-2}\Psi(x/a)$, and Ψ is an integrable function or measure on $I\!R^2$ with mean value 0 or, in other words, $\hat{\Psi}(0) = 0$. Note that by virtue of Plancherel's formula

$$W_\Psi f(a,x) = (2\pi)^{-2} \int_{\boldsymbol{R}^2} e^{i\langle x,\xi\rangle} \hat{\Psi}(a\xi)\hat{f}(\xi)d\xi\,.$$

So if the support of $\hat{\Psi}$ is the annulus $0 < b_0 \leq |\xi| \leq b_1 < \infty$, this is "roughly" the case for some b_0 and b_1 whenever Ψ is a smooth and integrable radial function with mean value zero, then $W_\Psi f(a,x)$ may be viewed as the frequency content of f in the band $b_0/a \leq |\xi| \leq b_1/a$ at x.

In theoretical applications, for example see [2, 14, 24], the specific Ψ is not really important, only certain of its properties play a major role. However, in numerical work it is nice to have explicit expressions for both Ψ and its Fourier transform. In addition to the Mexican hat wavelet mentioned earlier, typical examples are the following:

i Derivatives of the Poisson kernel

$$P_a(x) = \frac{a}{2\pi(a^2 + |x|^2)^{3/2}}$$

whose Fourier transform is

$$\widehat{P}_a(\xi) = e^{-a|\xi|}\,.$$

For instance

$$\Psi_a(x) = -a\frac{\partial P_a}{\partial a}(x) = \frac{2a^3 - a|x|^2}{2\pi(a^2 + |x|^2)^{5/2}}$$

whose Fourier transform is

$$\widehat{\Psi}_a(\xi) = |a\xi|e^{-|a\xi|}\,.$$

ii Appropriate differences of known summability kernels or measures. For instance

$$\Psi_a(x) = \delta(x) - P_a(x)$$

or

$$\Psi_a(x) = 2P_a(2x) - P_a(x)$$

where $P_a(x)$ is the Poisson kernel and $\delta(x) = a^{-2}\delta(x/a)$ is the bivariate normalized Dirac delta "function". In this case

$$\hat{\Psi}_a(\xi) = 1 - e^{-a|\xi|}$$

or

$$\hat{\Psi}_a(\xi) = e^{-a|\xi/2|} - e^{-a|\xi|}$$

respectively.

If Ψ is a radial function which is sufficiently smooth then it can be represented as a uniform sum of ridge functions, that is

$$\Psi(x) = \frac{1}{2\pi}\int_0^{2\pi} \psi(\langle x, u_\theta\rangle)d\theta \tag{22}$$

for some even univariate function $\psi(t)$. The significance of representation (22) lies in the fact that, for fixed θ, the (bivariate) convolution of $\psi(\langle x, u_\theta\rangle)$ with $f(x)$ can be expressed as the (univariate) convolution of $\psi(t)$ with $f_\theta(t)$ evaluated at $\langle x, u_\theta\rangle$. This leads to

$$\Psi_a * f(x) = \frac{1}{2\pi a}\int_0^{2\pi} \psi_a * f_\theta(\langle x, u_\theta\rangle)d\theta \tag{23}$$

where $\psi_a(t) = a^{-1}\psi(t/a)$. In short, (22) gives rise to a convenient formula, namely (23), for computing the wavelet transform of f with wavelet Ψ in terms of the Radon transform of f.

If Ψ and ψ satisfy (22) there are various alternate formulas relating Ψ to ψ, see [20]. A particularly convenient one relates their Fourier transforms,

$$2\hat{\psi}(|\xi|) = |\xi|\hat{\Psi}(\xi)\,. \tag{24}$$

whenever Ψ is a smooth function which decays sufficiently rapidly. Among other things, this formula implies that if Ψ is sufficiently smooth then ψ is integrable, has mean value zero, and

$$\psi_a * f_\theta(t)$$

is a (univariate) wavelet transform of f_θ. Thus in this case (23) implies that the (bivariate) wavelet transform of f is a sum of appropriately backprojected (univariate) wavelet transforms of the f_θ's, in other words,

$$W_\Psi f(a, x) = \frac{1}{2\pi a}\int_0^{2\pi} W_\psi f_\theta(a, \langle x, u_\theta\rangle)d\theta\,. \tag{25}$$

For example, the bivariate wavelet

$$\Psi_a(x) = \frac{2a^3 - a|x|^2}{2\pi(a^2 + |x|^2)^{5/2}}$$

mentioned earlier is related via (22) to the univariate wavelet

$$\psi_a(t) = \frac{a^5 - 3a^3t^2}{\pi(a^2 + t^2)^3}$$

with

$$\hat{\psi}_a(\tau) = \frac{a^2\tau^2 e^{-|a\tau|}}{2}.$$

Other examples are included in what follows.

2.6 A connection with local and pseudolocal tomography

According to the authors of [6, 7, 30], in practical applications of local tomography they do not compute $\Lambda f(x)$, rather they attempt to reconstruct $\Lambda(\Phi_\epsilon * f)(x)$ for some approximation of the identity $\Phi_\epsilon(x) = \epsilon^{-2}\Phi(x/\epsilon)$, $\epsilon > 0$, where Φ is an integrable function with total integral one. Now, for sufficiently well behaved Φ, $\Lambda\Phi$ is an integrable function with mean value zero, $\Lambda(\Phi_\epsilon) = \epsilon^{-1}(\Lambda\Phi)_\epsilon$, and we may write

$$\Lambda(\Phi_\epsilon * f)(x) = \epsilon^{-1}(\Lambda\Phi)_\epsilon * f(x)\,. \tag{26}$$

The last formula may be re-expressed as

$$\Lambda(\Phi_\epsilon * f)(x) = \epsilon^{-1} W_\Psi f(\epsilon, x) \tag{27}$$

where

$$\Psi(x) = \Lambda\Phi(x)\,. \tag{28}$$

In other words, $\epsilon\Lambda(\Phi_\epsilon * f)(x)$ with $a = \epsilon$ is a wavelet transform of f.

If Φ is a sufficiently well behaved radial function then, in view of (25), the wavelet transform suggested by (27) can be conveniently computed in terms of the Radon transform of f. Indeed the corresponding univariate wavelet ψ can, in certain cases, be easily determined from Φ. For example, by virtue of (24),

$$2\hat{\psi}(|\xi|) = |\xi|^2\widehat{\Phi}(\xi) \tag{29}$$

whenever relations (22) and (28) are valid and Ψ is sufficiently well behaved. In particular, if

$$\Phi(x) = \frac{1}{2\pi(1 + |x|^2)^{3/2}}$$

then $\Phi_\epsilon(x)$ is the so-called Poisson kernel for the upper half space $\{(x, \epsilon) : x \in I\!R^2 \text{ and } 0 < \epsilon < \infty\}$, (28) gives

$$\Psi(x) = \frac{2 - |x|^2}{2\pi(1 + |x|^2)^{5/2}},$$

and the relationship between Ψ and ψ results in the formula

$$\psi(t) = \frac{1 - 3t^2}{\pi(1+t^2)^3}.$$

This is essentially the example considered in Subsection **2.5**. The case

$$\Phi(x) = \frac{e^{-|x|^2/2}}{2\pi}$$

gives rise to

$$\psi(t) = \frac{(1-t^2)e^{-t^2/2}}{2\sqrt{2\pi}},$$

so the Gaussian kernel Φ_ϵ gives rise to

$$(\Lambda\Phi)_\epsilon f(x) = \frac{1}{2\pi\epsilon}\int_0^{2\pi} W_\psi f_\theta(\epsilon, \langle x, u_\theta\rangle)d\theta$$

where ψ is the univariate Mexican hat wavelet.

The expression $h_\epsilon f(x)$ from the "pseudolocal tomography" found in [12] is a wavelet transform of f with $a = \epsilon$ and

$$\Psi_\epsilon(x) = \delta(x) - k_\epsilon(x)$$

where $k_\epsilon(x)$ is described by the formulas immediately succeeding (11) and $\delta(x)$ is the bivariate normalized Dirac delta "function". Thus this analyzing wavelet Ψ_ϵ is a special case of the general form mentioned in example **ii** in previous subsection.

On the other hand, the authors of [12] also suggest the computation of

$$h_{\epsilon_1}(\Phi_{\epsilon_2} * f)(x)$$

for positive ϵ_1 and ϵ_2 in lieu of the computation of $h_\epsilon f(x)$. Since, by virtue of (19) and (11),

$$h_{\epsilon_1}(\Phi_{\epsilon_2} * f)(x) = (\Phi_{\epsilon_2} - k_{\epsilon_1} * \Phi_{\epsilon_2}) * f(x)$$

where $k_{\epsilon_1}(x)$ is the kernel in equation (11), it is clear that for suitably well behaved Φ this expression is some sort of wavelet transform. Indeed, if $\epsilon_1 = c\epsilon_2 = c\epsilon$ then

$$h_{\epsilon_1}(\Phi_{\epsilon_2} * f)(x) = \epsilon^{-1} W_\Psi f(\epsilon, x)$$

where $\Psi(x) = \Phi(x) - k_c * \Phi(x)$. If Φ is radial then this wavelet transform may, in theory, be computed in terms of the Radon transform of f in a manner similar to that suggested above. Furthermore, if ϵ is sufficiently small then one may use the approximation suggested by (21)

$$h_{\epsilon_1}(\Phi_{\epsilon_2} * f)(x) \approx \frac{c\epsilon}{\pi}\Lambda(\Phi_\epsilon * f)(x)$$

together with the formulas for computing $\Lambda(\Phi_\epsilon * f)(x)$.

Of course, similar remarks are also valid for $H_\epsilon f(x)$.

2.7 A wavelet transform for quasilocal tomography

Suppose

(30) $$\Psi(x) = K_{1/2}(x) - K_1(x)$$

where K_ϵ, $\epsilon = 1/2$ or 1, is the convolution kernel in Formula (14). This Ψ can also be described via

$$\Psi(x) = \frac{1}{\pi^2}\left\{\frac{1}{|x|} - \frac{\sqrt{|2x|^2-1}}{|x|^2}\chi(|2x|) + \frac{\sqrt{|x|^2-1}}{|x|^2}\chi(|x|)\right\}.$$

In view of (13) and (14) it follows that

(31)

$$\Psi_a * f(x) = \frac{-1}{8\pi^2}\int_0^{2\pi}\int_{a/2<|t|<a} \frac{f_\theta(\langle x,u_\theta\rangle+t) - 2f_\theta(\langle x,u_\theta\rangle) + f_\theta(\langle x,u_\theta\rangle - t)}{t^2} dt d\theta .$$

From (31) it is clear that the wavelet transform

$$W_\Psi f(a,x) = \Psi_a * f(x)$$

does not require knowledge of the full Radon transform of f, it can be computed in in terms of only those integrals of f over lines whose intersection with the disk $\{x : |x| < a\}$ is non-empty.

Viewed in terms of the material in Subsection **2.5** the function ψ corresponding to Ψ is the distribution

$$\psi(t) = \frac{1}{\pi}\left\{\delta(t) - \frac{\chi(2t) - \chi(t)}{2t^2}\right\}$$

where $\delta(t)$ is the univariate normalized Dirac delta "function" and $\chi(t)$ is the indicator function of the set $\{t : |t| > 1\}$. This is an immediate consequence of (31).

Observe that

$$\sum_{j=M+1}^{N} \Psi_{2^j\epsilon} * f(x) = K_{2^M\epsilon} * f(x) - K_{2^N\epsilon} * f(x)$$

for any integers $M < N$ and any positive ϵ. Since,

$$\lim_{M\to-\infty} K_{2^M\epsilon} * f(x) = f(x) \quad \text{and} \quad \lim_{N\to\infty} K_{2^N\epsilon} * f(x) = 0$$

it follows that

(32) $$f(x) = \sum_{j=-\infty}^{\infty} \Psi_{2^j\epsilon} * f(x).$$

In view of (31), formula (32) is an inversion formula for the Radon transform. Truncating (32) appropriately leads to approximate reconstruction formulas.

For example, If f is supported in the unit disk $\{x : |x| \leq 1\}$ then the integrand in formula (31) reduces to $-2f_\theta(\langle x, u_\theta\rangle)/t^2$ whenever $|x| \leq 1$ and $|t| > 2$. Hence if $|x| \leq 1$ it follows that

$$\Psi_a * f(x) = \frac{1}{2\pi^2 a}\int_0^{2\pi} f_\theta(\langle x, u_\theta\rangle)d\theta$$

whenever a is greater than 4. In this case formula (32) reduces to

$$f(x) = \frac{1}{2\pi^2 2^{N_0}\epsilon}\int_0^{2\pi} f_\theta(\langle x, u_\theta\rangle)d\theta + \sum_{j=-\infty}^{2} \Psi_{2^j\epsilon} * f(x) \tag{33}$$

where N_0 is the least integer so that $2^{N_0} > 4/\epsilon$. In numerical applications considerations of resolution impose natural truncation points for the last sum. See the next subsection.

Remark 1 It is important to note that the wavelet Ψ defined by (30) can be replaced with

$$K_{\epsilon_1}(x) - K_{\epsilon_2}(x)$$

for any ϵ_1 and ϵ_2 which satisfy $0 < \epsilon_1 < \epsilon_2$ with consequences analogous to those indicated above for the special case $\epsilon_1 = 1/2$ and $\epsilon_2 = 1$. This flexibility may be significant in numerical experiments and practical applications.

Remark 2 Of course many of the above observations are also valid if K is replaced by the kernel k in formula (11) or certain other kernels, including certain regularizations of k and K. However k is not as well behaved as K and, although other kernels may be better behaved, it is unlikely that the formula for the corresponding wavelet transform will be as simple as (31).

2.8 Discrete analogues

Suppose f is supported in the unit disk $\{x : |x| \leq 1\}$, we are given the discrete Radon transform data

$$Rf(\tfrac{m\pi}{M}, \tfrac{n}{N}),\ \ m = 0, 1, \ldots, M-1,\ \ n = 0, \pm 1, \pm 2, \ldots, \pm N, \tag{34}$$

and we wish to approximate

$$f(x) = \frac{-1}{8\pi^2}\int_0^{2\pi}\int_{-\infty}^{\infty} \frac{f_\theta(\langle x,u_\theta\rangle+t) - 2f_\theta(\langle x,u_\theta\rangle) + f_\theta(\langle x,u_\theta\rangle - t)}{t^2} dt d\theta \tag{35}$$

or

$$W_\Psi f(a,x) = \frac{1}{2\pi a}\int_0^{2\pi} \psi_a * f_\theta(\langle x, u_\theta\rangle)d\theta \tag{36}$$

where

$$\psi(t) = \frac{1}{\pi}\left\{\delta(t) - \frac{\chi(2t) - \chi(t)}{2t^2}\right\}.$$

Here $\delta(t)$ is the univariate normalized Dirac delta "function" and $\chi(t)$ is the indicator function of the set $\{t : |t| > 1\}$.

View the inner integral in either formula as the (univariate) convolution of an appropriate distribution w with f_θ and approximate the outer integration via the periodic trapezoid rule. This results in the approximation

$$c\frac{2\pi}{M}\sum_{m=0}^{M-1} w * f_{\theta_m}(\langle x, u_{\theta_m}\rangle) \tag{37}$$

where $\theta_m = \frac{m\pi}{M}$, $m = 0, 1, \ldots, M-1$, and c is the appropriate constant.

There are several ways to approximate the convolutions $w * f_{\theta_m}$. We use the paradigm suggested in [16]. Namely, first replace w with the distribution

$$\tilde{w}(t) = \sum_{n=-\infty}^{\infty} w_n \delta(t - \tfrac{n}{N}) \tag{38}$$

where $\delta(t)$ is the univariate unit Dirac delta "function" at the origin,

$$w_n = \int_{-\infty}^{\infty} w(t)\phi_n(t)dt\,,$$

and $\phi_n(t)$ is sufficiently smooth, is centered and concentrated around n/N, and has total integral one[8]. Next replace f_{θ_m} with

$$\tilde{f}_m(t) = \sum_{n=-N}^{N} f_{\theta_m}(\tfrac{n}{N})\lambda(t - \tfrac{n}{N}) \tag{39}$$

where λ is a continuous function which satisfies

$$\lambda(\tfrac{n}{N}) = \begin{cases} 1 & \text{if } n = 1 \\ 0 & \text{otherwise} \end{cases}$$

so that $\tilde{f}_m(t)$ is a continuous function which interpolates[9] $f_{\theta_m}(t)$ at $t = n/N$, $n = 0, \pm 1, \pm 2, \ldots$. Observe that

$$\tilde{w} * \tilde{f}_m(t) = \sum_{n=-\infty}^{\infty}\left\{\sum_{l=-N}^{N} w_{n-l} f_{\theta_m}(\tfrac{l}{N})\right\}\lambda(t - \tfrac{n}{N})\,. \tag{40}$$

[8] w_n is the distribution w evaluated at ϕ_n which, instead of the integral, may be more properly expressed as $w_n = \langle w, \phi_n\rangle$.

[9] λ should also be chosen so that $\tilde{f}_m(t)$ approximates $f_{\theta_m}(t)$ well.

noting that

$$\tilde{w} * \tilde{f}_m(\tfrac{n}{N}) = \sum_{l=-N}^{N} w_{n-l} f_{\theta_m}(\tfrac{l}{N})$$

and if λ has compact support then the sum in n in (40) has a finite number of non-zero terms.

Since $f_{\theta_m}(\frac{n}{N}) = Rf(\frac{m\pi}{M}, \frac{n}{N})$, the approximations suggested by (37) and (40) give rise to approximations of (35) and (36) which can be computed in terms of the discrete Radon transform data (34) of f.

For example, if

$$\phi_n(t) = N\phi(Nt - n) \tag{41}$$

where

$$\phi(t) = \begin{cases} 1 & \text{if } |t| \leq 1/2 \\ 0 & \text{otherwise,} \end{cases} \tag{42}$$

then the distribution w in (35) gives rise to

$$w_n = N \int_{-\infty}^{\infty} \frac{\phi(Nt - n) - 2\phi(n) + \phi(Nt + n)}{t^2} dt$$

which simplifies to

$$w_n = \frac{8N^2}{4n^2 - 1} \tag{43}$$

The resulting approximation Af of f is given by

$$Af(x) = \frac{N^2}{4\pi M} \sum_{m=0}^{M-1} \sum_{n=-\infty}^{\infty} \left\{ \sum_{l=-N}^{N} \frac{f_{\theta_m}(l/N)}{1 - 4(n-l)^2} \right\} \lambda(\langle x, u_{\theta_m} \rangle - \tfrac{n}{N}) \tag{44}$$

In the case

$$\lambda(t) = \begin{cases} 1 - N|t| & \text{if } |t| \leq \frac{1}{N} \\ 0 & \text{otherwise} \end{cases} \tag{45}$$

the algorithm suggested by (44) is the well known algorithm introduced in [28].

To approximate the wavelet transform (36) observe that the distribution $w = \psi_a$ in (36) and the ϕ in (41) give rise to

$$w_n = N \int_{a/2 \leq |t| < a} \frac{\phi(Nt - n) - 2\phi(n) + \phi(Nt + n)}{t^2} dt\,.$$

To simplify evaluation of this expression we choose a convenient relationship between the parameters a and N, namely,

$$a = \frac{2^\ell}{N} \tag{46}$$

for some integer ℓ, $\ell = 0, 1, 2, \ldots$. If (46) holds then

$$w_n = \begin{cases} -\frac{4N^2}{2^\ell} & \text{if } n = 0 \\ \frac{8N^2}{4n^2-1} & \text{if } 2^{\ell-1} < |n| < 2^\ell \\ \frac{4N^2}{2^\ell(2^\ell+1)} & \text{if } |n| = 2^{\ell-1} \\ \frac{4N^2}{2^{\ell+1}(2^{\ell+1}-1)} & \text{if } |n| = 2^\ell \\ 0 & \text{otherwise.} \end{cases} \tag{47}$$

Denote the train of δ functions with weights given by (47) as $\tilde{w}_a$ to indicate its dependence on a. Here a takes on the possible values $2^\ell/N$, $\ell = 0, 1, 2, \ldots$. Then

$$AW_\Psi f(a,x) = \frac{-1}{4\pi M} \sum_{m=0}^{M-1} \tilde{w}_a * \tilde{f}_m(\langle x, u_{\theta_m} \rangle) \tag{48}$$

is a natural approximation to a wavelet transform of f which is computable in terms of its Radon transform data (34). Furthermore, if $\lambda(t)$ is chosen to have small support such as (45) then $AW_\Psi f(a,x)$ depends only on integrals of f over lines which intersect the disc of radius a centered at x; more precisely, $AW_\Psi f(a,x)$ depends only on $Rf(m\pi/M, n/N)$ for $|\frac{n}{N} - \langle x, u_{m\pi/M} \rangle| \leq a$ and $m = 0, 1, \ldots, M-1$.

Finally, if we denote the train of δ functions with weights given by (43) as $\tilde{w}$, it is not difficult to see that

$$\tilde{w}(t) = \sum_{\ell=0}^{\infty} \tilde{w}_{2^\ell/N}(t)\,. \tag{49}$$

Relationship (49) is essentially a discrete analogue of (32). Using reasoning similar to that which led to (33) results in the approximation

$$Af(x) = \sum_{j=0}^{N_0} AW_\Psi f(2^j/N, x) + \frac{N}{\pi M 2^{N_0}} \sum_{m=0}^{M-1} \tilde{f}_m(\langle x, u_\theta \rangle)\,. \tag{50}$$

where N_0 is the smallest integer such that $2^{N_0} > 2N$. What is remarkable about this simple decomposition is the fact that often the first few terms of the first sum are sufficient to obtain a reasonable reconstruction. This is illustrated by Example 1 below.

Remark 1 Similar formulas are valid involving the more general Ψ's mentioned in Remark 1 at the end of the previous subsection. The significance of this lies in the fact that one may want to experiment with the various choices of parameters ϵ_1 and ϵ_2 to determine selections most suitable for specific applications.

Remark 2 The choice of ϕ suggested by (42) was motivated by the connection with the classical algorithm of Shepp and Logan [28]. However,

in view of the distribution w in (35) and (36), this choice seems somewhat less than ideal.

A smooth, yet extremely simple, selection is

$$\phi(t) = \begin{cases} 1 - 3t^2 + 2|t|^3 & \text{if } |t| \le 1 \\ 0 & \text{otherwise} \end{cases} \tag{51}$$

which is twice continuously differentiable, is supported in $\{t : |t| \le 1\}$ and satisfies

$$\phi(0) = 1, \quad \sum_{n=-\infty}^{\infty} \phi(t-n) = 1, \quad \text{and} \quad \int_{-\infty}^{\infty} \phi(t)dt = 1.$$

In this case the distribution $\tilde{w}$ corresponding to the w in (35) has the weights

(52)

$$w_n = c \begin{cases} 1 & \text{if } n = 0 \\ 1 - 2\log 2 & \text{if } |n| = 1 \\ 1 - (|n| + n^2)\log(\frac{|n|+1}{|n|}) - (|n| - n^2)\log(\frac{|n|}{|n|-1}) & \text{if } |n| \ge 2 \end{cases}$$

where c is an appropriately chosen constant. In other words, (52) is the analogue of (43) if (51) is used instead of (42).

The weights for the distributions $\tilde{w}_a$, $a = 2^\ell/N$, $\ell = 0, 1, 2 \ldots$, which may be used to approximate the wavelet transform (36) are the following: when $\ell = 0$ then

$$w_n = c \begin{cases} 3 & \text{if } n = 0 \\ -3/2 & \text{if } |n| = 1 \\ 0 & \text{if } |n| \ge 2\,; \end{cases}$$

when $\ell = 1$ then

$$w_n = c \begin{cases} 2 & \text{if } n = 0 \\ -16 - 24\log 2 & \text{if } |n| = 1 \\ 24\log 2 - 17 & \text{if } |n| = 2 \\ 0 & \text{if } |n| \ge 3\,; \end{cases}$$

and when $\ell \ge 2$ then

(53)

$$w_n = 2c \begin{cases} 1/2^\ell & \text{if } n = 0 \\ 6\{1-(|n|+n^2)\log(\frac{|n|+1}{|n|})-(|n|-n^2)\log(\frac{|n|}{|n|-1})\} & \text{if } 2^{\ell-1} < |n| < 2^\ell \\ -1/|n| + 3 + 6|n| - 6(|n| + n^2)\log(\frac{|n|+1}{|n|}) & \text{if } |n| = 2^{\ell-1} \\ 1/|n| + 3 - 6|n| - 6(|n| - n^2)\log(\frac{|n|}{|n|-1}) & \text{if } |n| = 2^\ell \\ 0 & \text{otherwise.} \end{cases}$$

where c is an appropriately chosen constant and is the same in all three formulas. In other words, (53) and the two preceding formulas[10] are the analogue of (47) if (51) is used instead of (42). The wavelet transforms in our numerical examples are computed with these weights.

2.9 Numerical examples

We present the results of two numerical experiments based on the algorithms suggested by the formulas in Subsection **2.8**. As is customary, we used the celebrated phantom Φ which was originally introduced and documented in [28]. That is, $\Phi(x)$ is the linear combination of indicator functions of ellipses as described in [28]. MATLAB software was used to implement the algorithms and display the results.

2.9.1 Example 1

The point of this example is to compare a classical reconstruction with that suggested by the discrete analogues of the wavelet transform.

We used the data described by (34) with $f(x) = \Phi(x)$, $M = 90$, and $N = 100$. The results are summarized by Figures 1-5. Each "reconstruction" was evaluated on a 201×201 grid determined by $x = (\frac{j_1-100}{100}, \frac{j_2-100}{100})$ and is represented by a matrix $I = (I_{j_2,j_1})$ where j_1 and j_2 take on the values $0, 1, \ldots, 200$. Each figure contains three plots.

- A plot of the "cross-section" I_{101,j_1}, $j_1 = 0, 1, \ldots, 200$.
- A plot of It_{101,j_1}, $j_1 = 0, 1, \ldots, 200$, where It is the range truncated variant of I defined by

$$It_{j_2,j_1} = \begin{cases} \mu_1 & \text{if } I_{j_1,j_1} \geq \mu_1 \\ I_{j_1,j_1} & \text{if } \mu_0 \leq I_{j_1,j_1} \leq \mu_1 \\ \mu_0 & \text{if } I_{j_1,j_1} \leq \mu_0 \,. \end{cases}$$

  The values of μ_0 and μ_1 were chosen so that the variations inside the "skull" would be visible and were determined experimentally by viewing the plot of I_{101,j_1} with different scalings on the vertical axis.

- A gray level representation (image) of It using 256 gray levels uniformly distributed between μ_0 and μ_1.

Figure 1 gives the results of the computation of $Af(x)$, the approximation of f given by formula (44). In other words, this is the result of applying

[10] Since all three formulas are special cases of one general formula we will refer to them collectively as (53) in what follows.

the celebrated Shepp-Logan algorithm [28]. It is presented for comparison purposes.

We computed the approximations $AW_\Psi f(2^j/N, x)$, $j = 0, 1, \ldots, 7$, to the wavelet transform using the algorithm suggested by (48) and the weights given by (53).

Figures 2, 3, and 4 show $AW_\Psi f(a, x)$ with $a = 1/N, 2/N$, and $4/N$ respectively. Figure 5 shows the reconstruction

$$Af(x) = \sum_{j=0}^{7} AW_\Psi f(2^j/N, x) + \frac{N}{\pi M 2^8} \sum_{m=0}^{M-1} \tilde{f}_m(\langle x, u_\theta \rangle) .$$

The algorithms for computing $Af(x)$ were not normalized so that the plots in Figures 1 and 5 should only be compared relatively not absolutely.

2.9.2 Example 2

The point of this example is to numerically illustrate the local nature of the wavelet transform $W_\Psi f(a, x)$ with Ψ as described by (30), when computed from Radon transform data.

We used the data

$$(54) \qquad Rf(\tfrac{m\pi}{M}, \tfrac{2n}{N}), \quad m = 0, 1, \ldots, M-1, \quad n = 0, \pm 1, \pm 2, \ldots, \pm N,$$

with $f(x) = \Phi(x + x_0)$, $M = 90$, and $N = 200$. Here $x_0 = (0, -.605)$ is the center of the central small ellipse in the lower portion of the original phantom Φ. We computed "reconstructions" from from various truncations of the data matrix, $D_{m,n} = Rf(\frac{m\pi}{M}, \frac{2n}{N})$, in the second variable; more specifically $n = 0, \pm 1, \pm 2, \ldots, \pm rN$, with $r = 1, 3/4, 1/2, 1/4$, and $1/8$.

The results are summarized in Figures 6-10 and 11-15.

Each "reconstruction" was evaluated on a 401×401 grid determined by $x = (\frac{(j_1-200)r}{100}, \frac{(j_2-200)r}{100})$ and is represented by a matrix $I = (I_{j_2,j_1})$ where j_1 and j_2 take on the values $0, 1, \ldots, 400$. Each of the Figures 6-10 contains three plots.

- A gray level representation (image) of the data using 256 gray levels uniformly distributed between 0 and the maximum of the data.

- A gray level representation (image) of the truncated matrix It, with values between μ_0 and μ_1, which represents the result of simply applying the Shepp-Logan algorithm (formula (44)) to the data; 256 gray levels uniformly distributed between μ_0 and μ_1 were used. The range truncated matrix It was obtained by essentially the same procedure as described in Example 1; namely the values of μ_0 and μ_1 were chosen so that the variations inside the "skull" would be visible and were determined experimentally by viewing the plot of I_{201,j_1} with different

scalings on the vertical axis. See Figures 11-15. In the case $r = 1/8$ it was impossible to find appropriate values of μ_0 and μ_1; the case $r = 1/4$ was at best borderline.

- A gray level representation (image) of the truncated matrix It, with values between μ_0 and μ_1, which represents $AW_\Psi f(1/N, x)$ as computed by the algorithm suggested by (48) and the weights given by (53); 256 gray levels uniformly distributed between μ_0 and μ_1 were used. The range truncated matrix It was obtained as described in the previous item. Note that even in the cases $r = 1/4$ and $1/8$ it was possible to find appropriate values of μ_0 and μ_1.

Figures 6-8 are scaled so that they occupy the same area. Figures 8-10 are scaled in correct proportion.

Figures 11-15 contain the central "cross-sections" of the reconstructions found in Figures 6-10 respectively and document how the range truncated matricies It were obtained. Each figure, call it by it's number figure number, consists of four plots arranged as

$$\begin{array}{cc} 1 & 3 \\ 2 & 4 \end{array}$$

and which contain, respectively, the following.

1. A plot of the "cross-section" I_{201,j_1}, $j_1 = 0, 1, \ldots, 400$, where the 401×401 matrix I represents the result of simply applying the Shepp-Logan algorithm (formula (44)) to the corresponding data in Figure $n - 5$.

2. A plot of It_{201,j_1}, $j_1 = 0, 1, \ldots, 400$, where It is the range truncated variant of the matrix I defined in item 1. As mentioned earlier, this truncation was obtained in the same manner as indicated in Example 1.

3. A plot of the "cross-section" I_{201,j_1}, $j_1 = 0, 1, \ldots, 400$, where the 401×401 matrix I represents $AW_\Psi f(1/N, x)$ as computed from the data in Figure $n - 5$ by the algorithm suggested by (48) and the weights given by (53).

4. A plot of It_{201,j_1}, $j_1 = 0, 1, \ldots, 400$, where It is the range truncated variant of the matrix I defined in item 3. Again, this truncation was obtained in the same manner as indicated in Example 1.

3 Details

3.1

To see that $F_x(t)$ is the average of the integrals of f over lines which are a distance $|t|$ from x simply write

$$2\pi F_x(t) = \int_0^{2\pi} \int_{-\infty}^{\infty} f(\{\langle x, u_\theta \rangle + t\}u_\theta + sv_\theta) ds d\theta$$

$$= \int_0^{2\pi} \int_{-\infty}^{\infty} f(\{\langle x, u_\theta \rangle + t\}u_\theta + \{\langle x, v_\theta \rangle + s\}v_\theta) ds d\theta$$

because the integration in s is translation invariant. Since $x = \langle x, u_\theta \rangle u_\theta + \langle x, v_\theta \rangle v_\theta$, we may write

$$F_x(t) = \frac{1}{2\pi} \int_0^{2\pi} \left\{ \int_{-\infty}^{\infty} f(x + tu_\theta + sv_\theta) ds \right\} d\theta$$

which is the desired result since the expression in braces is the integral of f over the line which is t units away from x in the direction u_θ.

3.2

The formal adjoint of R is the transformation $R^\#$ which maps suitably well behaved scalar valued functions $f^*(\theta, t)$ on $[0, 2\pi) \times I\!R$ to functions $R^\# f^*(x)$ on $I\!R^2$ and satisfies the relation

$$\int_{I\!R^2} f(x) R^\# f^*(x) dx = \int_0^{2\pi} \int_{-\infty}^{\infty} Rf(\theta, t) f^*(\theta, t) dt d\theta \,.$$

Routine calculations, namely

$$\int_0^{2\pi} \int_{-\infty}^{\infty} Rf(\theta, t) f^*(\theta, t) dt d\theta = \int_0^{2\pi} \int_{-\infty}^{\infty} \int_{-\infty}^{\infty} f(tu_\theta + sv_\theta) f^*(\theta, t) ds dt d\theta$$

$$= \int_0^{2\pi} \int_{I\!R^2} f(x) f^*(\theta, \langle x, u_\theta \rangle) dx d\theta$$

where $t = \langle x, u_\theta \rangle$ and $s = \langle x, v_\theta \rangle$, show that

$$R^\# f^*(x) = \int_0^{2\pi} f^*(\theta, \langle x, u_\theta \rangle) d\theta \,.$$

To see that $R^\# Rf = 4\pi J * f$ write

$$R^\# Rf(x) = \int_0^{2\pi} f_\theta(\langle x, u_\theta \rangle) d\theta = \int_0^{2\pi} \int_{-\infty}^{\infty} f(\langle x, u_\theta \rangle u_\theta + sv_\theta) ds d\theta \,.$$

Because the inner integral is translation invariant the variable s may be replace by $\langle x, v_\theta \rangle + s$ which, in view of the fact that $x = \langle x, u_\theta \rangle u_\theta + \langle x, v_\theta \rangle v_\theta$, results in

$$\begin{aligned} R^{\#}Rf(x) &= \int_0^{2\pi} \int_{-\infty}^{\infty} f(x + sv_\theta) ds d\theta \\ &= 2 \int_0^{2\pi} \int_0^{\infty} \frac{f(x - su_\theta)}{s} s ds d\theta \\ &= \int_{\boldsymbol{R}^2} \frac{2}{|y|} f(x - y) dy \end{aligned}$$

when the polar change of variables $y = su_\theta$ is used.

The fact that the Fourier transform of $|x|^{-1}$ is a constant multiple of itself follows from elementary fact that the bivariate Fourier transform of a radial distribution homogeneous of degree minus one is a radial distribution homogeneous of degree minus one. The value of the constant follows from the Fourier inversion formula

$$f(x) = \frac{1}{(2\pi)^2} \int_{\boldsymbol{R}^2} \hat{f}(\xi) e^{i\langle x, \xi \rangle} d\xi \,.$$

Recall that the Laplacian Δ is the differential operator defined by

$$\Delta f(x) = \frac{\partial^2 f}{\partial x_1^2}(x) + \frac{\partial^2 f}{\partial x_2^2}(x)$$

whose Fourier transform is

$$\widehat{\Delta f}(\xi) = -|\xi|^2 \hat{f}(\xi) \,.$$

In view of this all the formulas involving Λ and Λ^{-1} are routine consequences of previous identities.

3.3

Formula (12) is not equivalent to (1). However it is a natural consequence of certain summability formulas for the inversion of the Radon transform. The details can be found in [20, page 196] and [21].

The formulas $g_\epsilon f(x) = k_\epsilon * f(x)$ and $G_\epsilon f(x) = K_\epsilon * f(x)$ follow from the identities

$$\int_0^{2\pi} f_\theta(\langle x, u_\theta \rangle - t) d\theta = 2 \int_{|y|>|t|} \frac{f(x - y)}{\sqrt{|y|^2 - t^2}} dy \,, \tag{55}$$

$$\int_0^{2\pi} \int_{|t|>\epsilon} \frac{f_\theta(\langle x, u_\theta \rangle)}{t^2} dt d\theta = \frac{4}{\epsilon} \int_{\boldsymbol{R}^2} \frac{1}{|y|} f(x - y) dy \,, \tag{56}$$

and

$$(57)\qquad \int_0^{2\pi}\int_{|t|>\epsilon}\frac{f_\theta(\langle x,u_\theta\rangle - t)}{t^2}dtd\theta = 4\int_{|y|>\epsilon}\frac{\sqrt{|y/\epsilon|^2-1}}{|y|^2}f(x-y)dy\,.$$

Let $I_1(t)$, $I_2(\epsilon)$, and $I_3(\epsilon)$ denote the right hand sides of formulas (55), (56), and (57) respectively. Note that $I_1(t)$ and $I_3(\epsilon)$ can also be expressed as

$$I_1(t) = \int_0^{2\pi} f_\theta(\langle x,u_\theta\rangle + t)d\theta$$

and

$$I_3(\epsilon) = \int_0^{2\pi}\int_{|t|>\epsilon}\frac{f_\theta(\langle x,u_\theta\rangle + t)}{t^2}dtd\theta$$

or

$$I_3(\epsilon) = 2\int_0^{2\pi}\int_{\epsilon}^{\infty}\frac{f_\theta(\langle x,u_\theta\rangle + t)}{t^2}dtd\theta\,.$$

Thus

$$g_\epsilon f(x) = \frac{1}{2\pi^2}\left\{\frac{I_1(\epsilon)}{\epsilon} - \frac{I_3(\epsilon)}{2}\right\}$$

$$= \int_{|y|>\epsilon}\frac{1}{\epsilon^2\pi^2}\left\{\frac{1}{\sqrt{|y/\epsilon|^2-1}} - \frac{\sqrt{|y/\epsilon|^2-1}}{|y/\epsilon|^2}\right\}f(x-y)dy$$

$$= k_\epsilon * f(x)$$

and

$$G_\epsilon f(x) = \frac{-1}{8\pi^2}\{2I_3(\epsilon) - 2I_2(\epsilon)\}$$

$$= \int_{\boldsymbol{R}^2}\frac{1}{\epsilon^2\pi^2}\left\{\frac{1}{|y/\epsilon|} - \frac{\sqrt{|y/\epsilon|^2-1}}{|y/\epsilon|^2}\chi(y/\epsilon)\right\}f(x-y)dy$$

$$= K_\epsilon * f(x)$$

which are the desired results.

Formula (56) is simply a consequence of

$$\int_0^{2\pi} f_\theta(\langle x,u_\theta\rangle)d\theta = \int_{\boldsymbol{R}^2}\frac{2}{|y|}f(x-y)dy$$

and

$$\int_{|t|>\epsilon}\frac{dt}{t^2} = \frac{2}{\epsilon}\,.$$

To see formula (57) use identity (55) to write

$$\int_0^{2\pi}\int_{|t|>\epsilon}\frac{f_\theta(\langle x,u_\theta\rangle - t)}{t^2}dtd\theta = 2\int_{|t|>\epsilon}\int_{|y|>|t|}\frac{f(x-y)}{t^2\sqrt{|y|^2-t^2}}dydt$$

$$= 2\int_{|y|>\epsilon} \left\{ \int_{|y|>|t|>\epsilon} \frac{dt}{t^2\sqrt{|y|^2-t^2}} \right\} f(x-y)dy$$

$$= 2\int_{|y|>\epsilon} \frac{2\sqrt{|y/\epsilon|^2-1}}{|y|^2} f(x-y)dy\,,$$

which is the desired result.

Finally, to see (55) first recall, from Subsection **3.1**, that

$$\int_0^{2\pi} f_\theta(\langle x, u_\theta\rangle - t)d\theta = \int_0^{2\pi}\int_{-\infty}^{\infty} f(x - tu_\theta + sv_\theta)dsd\theta\,.$$

Now

$$-tu_\theta + sv_\theta = -\sqrt{t^2+s^2}(\alpha\cos\theta + \beta\sin\theta, \alpha\sin\theta - \beta\cos\theta)$$

where

$$\alpha = \frac{t}{\sqrt{t^2+s^2}} = \cos\phi \text{ and } \beta = \frac{s}{\sqrt{t^2+s^2}} = \sin\phi$$

so that

$$-tu_\theta + sv_\theta = -\sqrt{t^2+s^2}(\cos(\theta-\phi), \sin(\theta-\phi)) = -\sqrt{t^2+s^2}u_{\theta-\phi}\,.$$

Thus we may write

$$\int_0^{2\pi}\int_{-\infty}^{\infty} f(x - tu_\theta + sv_\theta)dsd\theta = \int_{-\infty}^{\infty}\int_0^{2\pi} f(x - \sqrt{t^2+s^2}u_{\theta-\phi})d\theta ds$$

$$= \int_{-\infty}^{\infty}\left\{\int_0^{2\pi} f(x - \sqrt{t^2+s^2}u_\theta)d\theta\right\} ds,$$

$$= 2\int_0^{2\pi}\left\{\int_0^{\infty} f(x - \sqrt{t^2+s^2}u_\theta)ds\right\} d\theta,$$

$$= 2\int_0^{2\pi}\left\{\int_{|t|}^{\infty} f(x - ru_\theta)\frac{rdr}{\sqrt{r^2-t^2}}\right\} d\theta,$$

$$= 2\int_{|y|>|t|} \frac{f(x-y)}{\sqrt{|y|^2-t^2}}dy$$

where the second equality follows from translation invariance in the θ variable, the third is a consequence of the fact that the integrand is even in s variable, the fourth is a result of the change of variable $r = \sqrt{t^2+s^2}$, and the last follows from the polar change of variable $y = ru_\theta$. This implies (55) and completes the proof of the formulas $g_\epsilon f(x) = k_\epsilon * f(x)$ and $G_\epsilon f(x) = K_\epsilon * f(x)$.

As mentioned earlier the various assertions of the Theorem are routine consequences of the representation $G_\epsilon f = K_\epsilon * f$ and the properties of K. More specifically:

- Statements **ii**, **iii**, and **iv** are well known consequences of the fact that K is integrable and $\int_{R^2} K(x)dx = 1$.

- Statement **v** follows from the additional fact that $\int_{R^2} |x|^\alpha |K(x)|dx$ is finite if $0 < \alpha < 1$ and $|x||K(x)| \leq C|x|^{-2}$ for $|x| > 2$.

- Assertion **vi** follows from the yet additional fact that K is a positive radial function.

- Statement **vii** follows from the general theory of Hölder classes of functions and the fact that

$$\int_{R^2} |K(x+y) - 2K(x) + K(x-y)|^q dx \leq C|y|^{2-q}$$

  if $1 \leq q < 2$, where C is a constant independent of y. For example see [2, 14, 24, 31].

- Finally, **i** follows from the facts that $\int_{R^2} K(x)dx = 1$ and that $|K(x)|$ is dominated by a integrable radially decreasing function, see [31]. Note that $k(x)$ does not enjoy the second property.

3.4

There are many ways of arriving at (16). Perhaps the most direct and simplest method is to use (i) the fact that the (univariate) Fourier transform of f_θ is equal to the (bivariate) Fourier transform of f restricted to the line τu_θ, $-\infty < \tau < \infty$, or symbolically $\hat{f}_\theta(\tau) = \hat{f}(\tau u_\theta)$, (ii) the Fourier inversion formula, and (iii) a polar change of variables. For example see [22, 29]. It is also a natural consequence of various summability formulas for the inversion of the Radon transform, see [20, page 196]. Of course it can also be derived from (1) by using the fact that

$$f_\theta(t) = f_{\theta+\pi}(-t)$$

and an interchange of order of differentiation and integration.

Reasonable smoothness conditions on f needed to make formula (16) valid are not clear. Certainly $f \in C^{1+\alpha}$ for some positive α is sufficient[11] but is far too restrictive for typical applications. For this reason we take (19) to be the definition of $h_\epsilon f(x)$ and view (18) as an expression valid for sufficiently smooth f.

[11] $C^{1+\alpha}$ is the class of those differentiable functions whose derivatives are Hölder continuous of order α.

3.5

Relationship (22) is valid whenever Ψ is a reasonably smooth radial function, it need not necessarily be integrable. Indeed, in [20] this relationship is systematically exploited with polynomial Ψ's.

On the other hand, (24) need not even make sense if Ψ is not integrable. Nevertheless if Ψ and sufficiently many of its derivatives are integrable then not only is ψ well defined by (24) but it is also integrable and has mean value zero. In this case, even if Ψ fails to be an analyzing wavelet because $\Psi(0) \neq 0$, the corresponding ψ is always a univariate analyzing wavelet. Thus if Ψ_a is a well behaved approximation of the identity (23) implies that $\Psi_a * f(x)$ can be computed as an average of wavelet transforms of f_θ, $0 \leq \theta < \pi$, and consequently (23) may be regarded as an approximate inversion formula in terms of wavelet transforms.

3.6

The way (26) is computed in terms of the Radon transform data of f is dictated by formula (8) and

$$(\Phi_\epsilon * f)_\theta(t) = (\Phi_\epsilon)_\theta * f_\theta(t)\,.$$

This results in

$$\Lambda(\Phi_\epsilon * f)(x) = -\frac{1}{4\pi}\int_0^{2\pi} (\Phi_\epsilon)''_\theta * f(\langle x, u_\theta\rangle)d\theta\,.$$

For more details see [7, 13, 30]. Thus

$$\psi_\epsilon(t) = -\frac{\epsilon^2}{2}(\Phi_\epsilon)''_\theta(t)$$

which is another variant of (29).

3.7

To see the formula for ψ observe that for any sufficiently well behaved univariate function g

$$\begin{aligned}
\psi_a * g(s) &= \frac{-a}{4\pi}\int_{a/2\leq t<a} \frac{g(s+t)-2g(s)+g(s-t)}{t^2}dt \\
&= \frac{g(s)}{\pi} - \frac{a}{2\pi}\int_{a/2\leq t<a} \frac{g(s-t)}{a^2(t/a)^2}dt \\
&= \frac{g(s)}{\pi} - \tilde{\psi}_a * g(s)
\end{aligned}$$

where

$$\tilde{\psi}(t) = \frac{\chi(2t) - \chi(t)}{2\pi t^2},$$

$\tilde{\psi}_a(t) = a^{-1}\tilde{\psi}(t/a)$, and $\chi(2t) - \chi(t)$ is the indicator function of $\{t : 1/2 < |t| \leq 1\}$.

3.8

There are several points of view concerning convolution-backprojection type reconstruction algorithms in computed tomography, [4, 6, 10, 13, 20, 22, 23, 27, 28, 29, 30]. We will not outline them all here and only mention that the connection between the various discrete implementations and the inversion methods on which they are based have, to my knowledge, not been definitively developed. These connections are usually based on well established, but nevertheless heuristic, principles rather than precise error estimates. The relatively recent papers [6, 23] nicely illustrate the state of the art.

For example, the artifacts introduced by discretization in the θ variable of the commonly used inversion methods are well known. However, they have not been quantitatively analyzed. On the other hand, the reconstruction algorithms introduced in [15, 17] do not give rise to such artifacts, indeed this is one of the central points of that work. Unfortunately, unlike some of the other methods described here, these algorithms have no localized analogues.

Since [16] may not be easily accessible, we now briefly outline the rationale for the paradigm used to approximate

$$w * g(s) = \int_{-\infty}^{\infty} w(s-t)g(t)dt$$

where w is a known univariate integrable function or measure, whose derivative is very large or even non-existant in the classical sense, and g is a univariate function supported in the interval $-1 \leq t \leq 1$ whose samples $g(n/N)$, $n = 0, \pm 1, \pm 2, \ldots, \pm N$, are known.

First assume that g is reasonably well behaved so that approximation

$$\tilde{g}(t) = \sum_{n=-N}^{N} g(n/N)\lambda(t - n/N)$$

enjoys the correct order of approximation. For example, if g is Hölder continuous of order α then

$$|g(t) - \tilde{g}(t)| \leq \frac{C}{N^\alpha}. \tag{58}$$

The primary rationale of this method is that the approximant be easy to compute and that the approximation of $w * g$ be of the same order as $|g(t) -$

$\tilde{g}(t)|$, e. g. (58). Now, consider the method outlined in Subsection 2.8, that is, replace w with

$$\tilde{w}(t) = \sum_{n=-\infty}^{\infty} w_n \delta(t - \tfrac{n}{N})$$

where $\delta(t)$ is the univariate unit Dirac delta "function" at the origin,

$$w_n = \int_{-\infty}^{\infty} w(t)\phi_n(t)dt\,,$$

and $\phi_n(t)$ is sufficiently smooth, is centered and concentrated around n/N, and has total integral one. It is not difficult to see that (i) $\tilde{w} * \tilde{g}$ is of the same form as $\tilde{g}$, that is, it is a linear combination of translates of λ, (ii) if the ϕ_n's are chosen appropriately then $\tilde{w} * \tilde{g}$ is easy to compute, and (iii) $|w * g(t) - \tilde{w} * \tilde{g}(t)|$ is of the same order as $|g(t) - \tilde{g}(t)|$, e. g. if (58) is the case then

$$|w * g(t) - \tilde{w} * \tilde{g}(t)| \leq \frac{LC}{N^{\alpha}}\,,$$

where L is the L^1 norm or total variation of w.

References

[1] M. Bhatia, W.C. Karl, and A.S. Willsky, A wavelet based method for multiscale tomographic reconstruction, *IEEE Trans. Med. Imag.*, 15 (1996), 92-101.

[2] J. Boman and H.S. Shapiro, Comparison theorems for generalized modulus of continuity, *Ark. för Math.* 9 (1971), 71-116.

[3] I. Daubechies, *Ten Lectures on Wavelets,* CBMS-NSF Regional Conference Series in Applied Mathematics, Vol 61, SIAM, Philadelphia, 1992.

[4] S. R. Deans, *The Radon Transform and some of its Applications*, Wiley, New York, 1983.

[5] J. DeStefano and T. Olsen, Wavelet localization of the Radon transform in even dimensions, *IEEE Trans. Signal Proc.*, Vol. 42, no. 8, (1994),

[6] A. Faridani, F. Keinert, F. Natterer, E.L. Ritman, and K.T. Smith, Local and global tomography, in *Signal Processing Part II: Control and Applications*, F.A. Grunbaum, J.W. Helton, and P. Khargonekar eds., The IMA Volumes in Mathematics and Its Applications, Vol. 23, Springer Verlag, New York, 1990, 241-255.

[7] A. Faridani, E.L. Ritman, and K.T. Smith, Local tomography, *SIAM J. Appl. Math.*, Vol. 52, No. 2, (1992), 459-484.

[8] S. Helgason, *The Radon Transform*, Birkhauser, Boston, 1980.

[9] C. E. Heil and D. F. Walnut, Continuous and Discrete Wavelet Transforms, SIAM Review 31-4 (1989), 628-666.

[10] G. T. Herman, *Image Reconstruction from Projections. The Fundamentals of Computerized Tomography*, Academic Press, 1980.

[11] M. Holschneider, Inverse Radon transform through inverse wavelet transforms, *Inverse Problems*, 7 (1991), 853-861.

[12] A. I. Katsevich and A. Ramm, Pseudolocal Tomography, *SIAM J. Appl. Math.*, 56 (1996), 167-191.

[13] J. V. Leahy, K. T. Smith and D. C. Solmon, Uniqueness, Nonuniqueness and Inversion in the X-ray and Radon Problems, *Proc. International Symposium on Ill-posed Problems*, Newark, DE, October 1979.

[14] W. R. Madych and N. M. Riviere, Multipliers of the Hölder classes, *J. Funct. Anal.* 21 (1976), 369-379.

[15] W. R. Madych, Degree of approximation in computerized tomography, *Approximation Theory III*, E.W. Cheney, ed., Academic, New York, 1980, 615-622.

[16] W. R. Madych and S. A. Nelson, Discrete convolution: function representation and error estimates, ISU preprint 1983.

[17] W. R. Madych and S. A. Nelson, Polynomial based Algorithms for Computed Tomography, *SIAM J.Appl.Math.*, 43 (1983), 193-208.

[18] W. R. Madych and S. A. Nelson, Polynomial based Algorithms for Computed Tomography, II, *SIAM J.Appl.Math.*, 44 (1984), 193-208.

[19] W. R. Madych, Limits of dilated convolution transforms, *SIAM J. Math. Anal.* 16 (1985), 551-558.

[20] W. R. Madych, Summability and approximate reconstruction from Radon transform data, *Contemporary Mathematics*, Vol. 113 (1990), 189-219.

[21] W. R. Madych, Pointwise inversion of the Radon transform, Preprint 1996.

[22] F. Natterer, *The Mathematics of Computerized Tomography*, John Wiley & Sons, Stuttgart, 1986.

[23] F. Natterer and A. Faridani, Basic algorithms in tomography, in same volume as [6], 321-333.

[24] J. Peetre, On the theory of $\mathcal{L}_{p,\lambda}$ spaces, *J. Funct. Anal.* 4 (1969), 71-87.

[25] J. Radon, Über die Bestimmung vo Funktionen durch ihre Integralwerte längs gewisser Mannigfaligkeiten, *Ber. Verh. Sächs. Akad. Wiss. Leipzig*, Math. Nat. kl. 69 (1917), 262-277.

[26] F. Rashid-Farrokhi, K.J.R. Liu, C.A. Berenstein, and D. Walnut, Wavelet-based multiresolution local tomography, 1996 preprint.

[27] H. J. Scudder, Introduction to Computer Aided Tomography, *Proc. IEEE*, 66 (1978), 628-637.

[28] L. A. Shepp and B. F. Logan, The Fourier reconstruction of a head section, *IEEE Trans. Nucl. Sci.*, NS-21-3 (1974), 24-43.

[29] L. A. Shepp and J. B. Kruskal, Computerized tomography: the new medical X-ray technology, *Amer. Math. Monthly*, 85 (1978), 420-439.

[30] K.T. Smith and F. Keinert, Mathematical foundations of computed tomography, *Applied Optics*, 24 (1985), 3950-3957.

[31] E. M. Stein, *Singular Integrals and Differentiability Properties of Functions*, Princeton Univ. Press, Princeton, N.J. 1970.

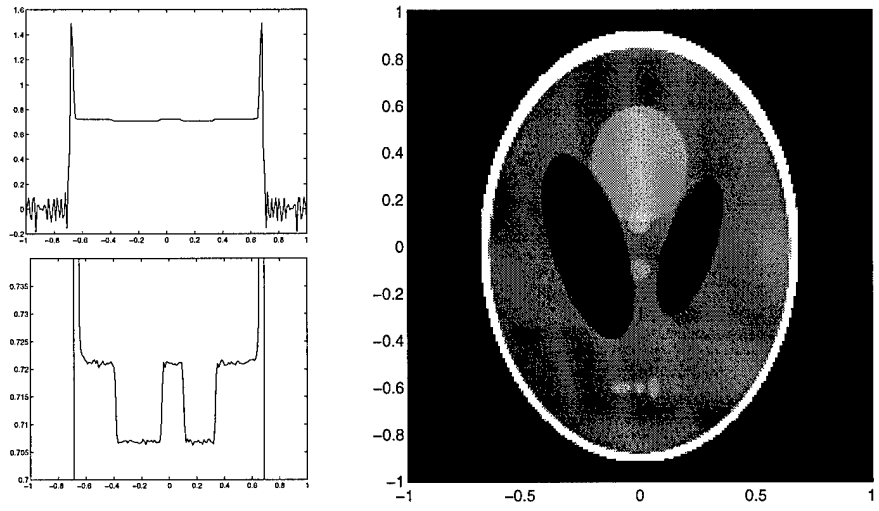

Figure 1: The reconstruction $Af(x)$ via formula (43).

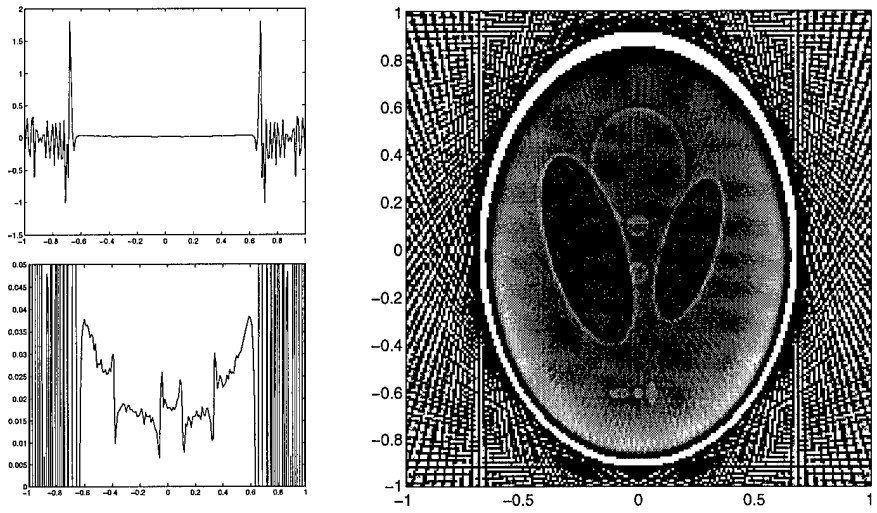

Figure 2: The wavelet transform $AW_\Psi f(1/N, x)$ via (47) using weights (53).

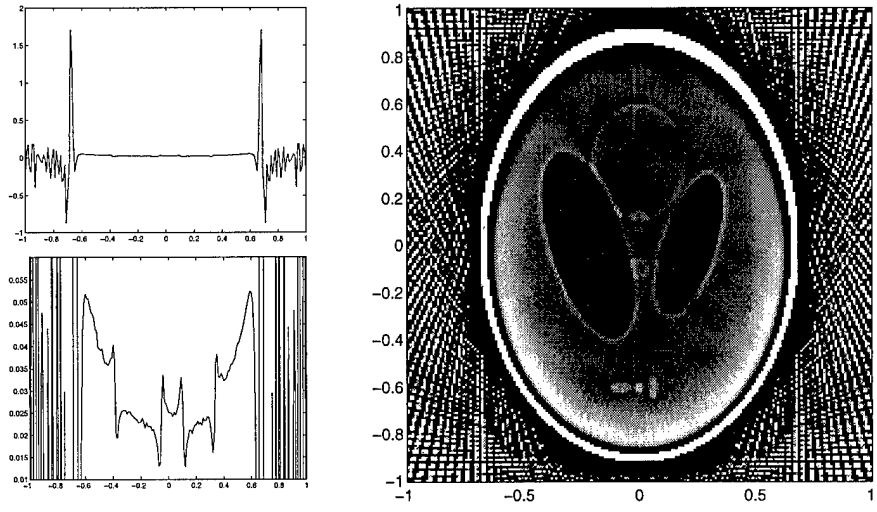

Figure 3: The wavelet transform $AW_\Psi f(2/N, x)$ via (47) using weights (53).

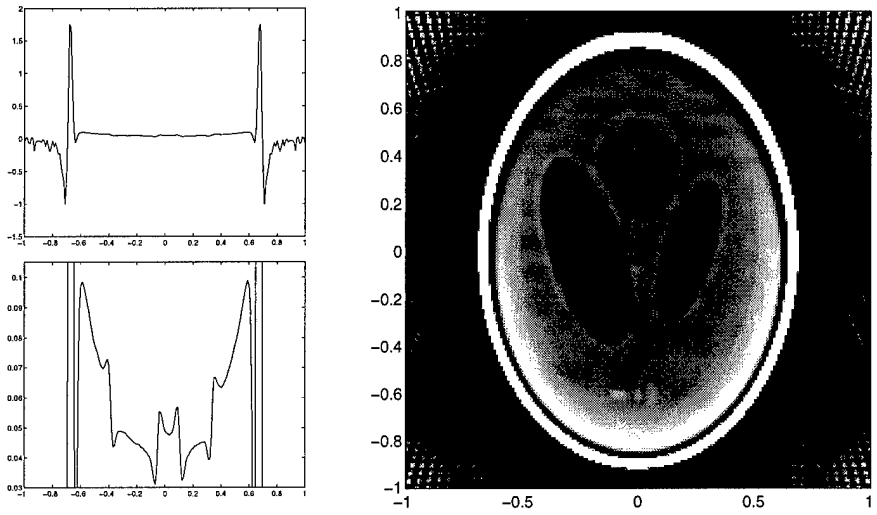

Figure 4: The wavelet transform $AW_\Psi f(4/N, x)$ via (47) using weights (52).

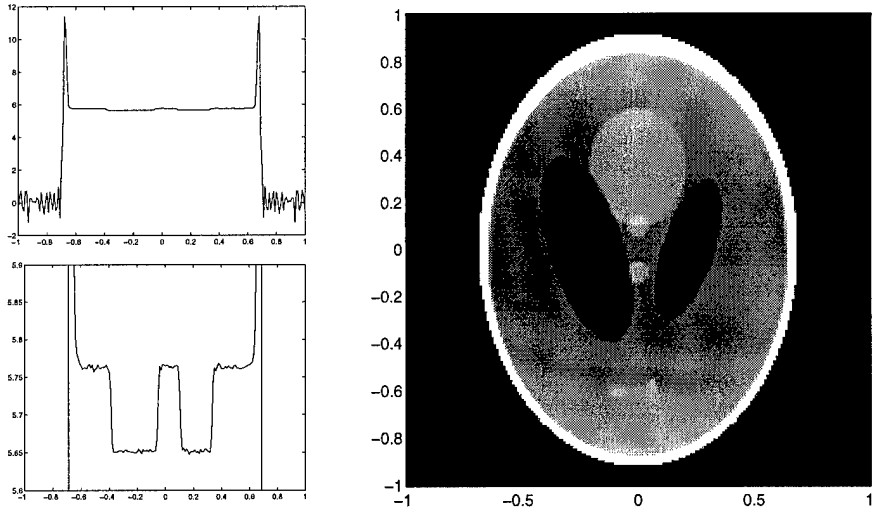

Figure 5: The reconstruction $Af(x)$ via (49) using weights (53) and $N_0 = 7$.

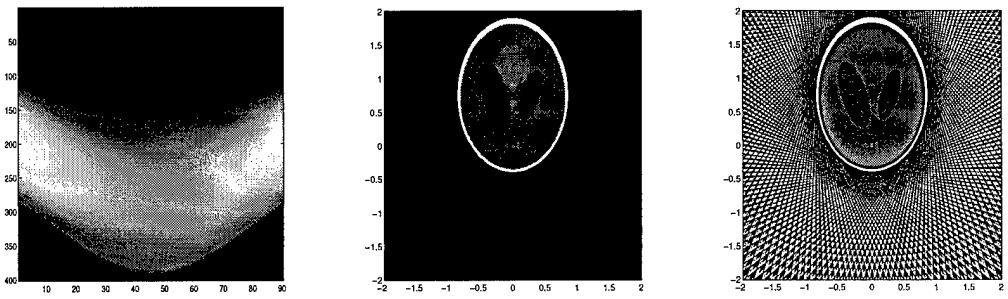

Figure 6: Full data, conventional reconstruction, and local wavelet transform

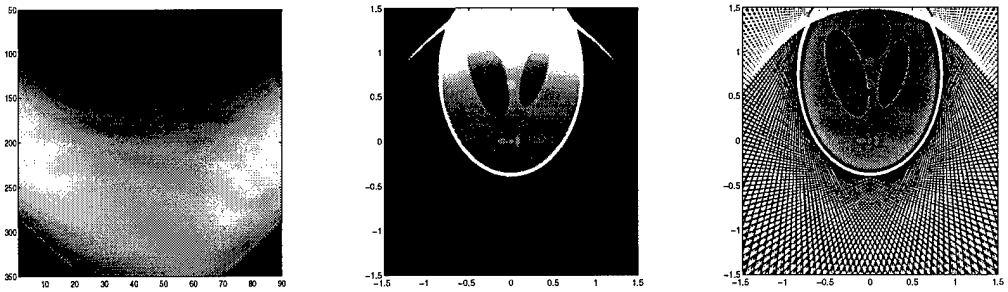

Figure 7: 3/4 of full data, conventional reconstruction, and local wavelet transform. Scaled to occupy the same area as Figure 6.

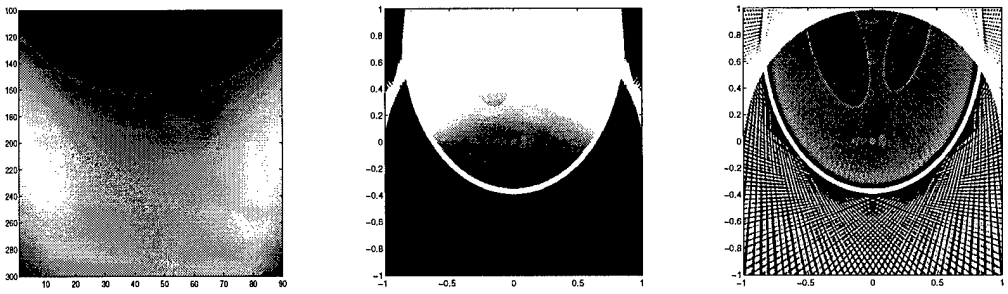

Figure 8: 1/2 of full data, conventional reconstruction, and local wavelet transform. Scaled to occupy the same area as Figure 6.

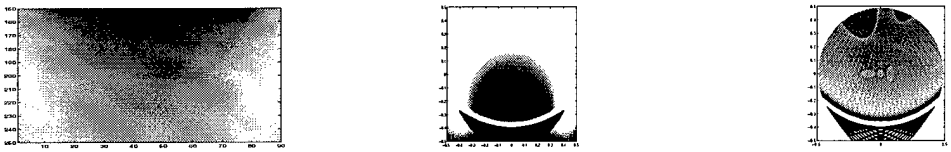

Figure 9: 1/4 of full data, conventional reconstruction, and local wavelet transform. Scaled to be proportional to Figure 8.

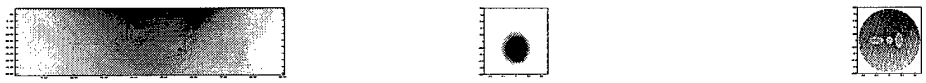

Figure 10: 1/8 of full data, conventional reconstruction, and local wavelet transform. Scaled to be proportional to Figures 8 and 9.

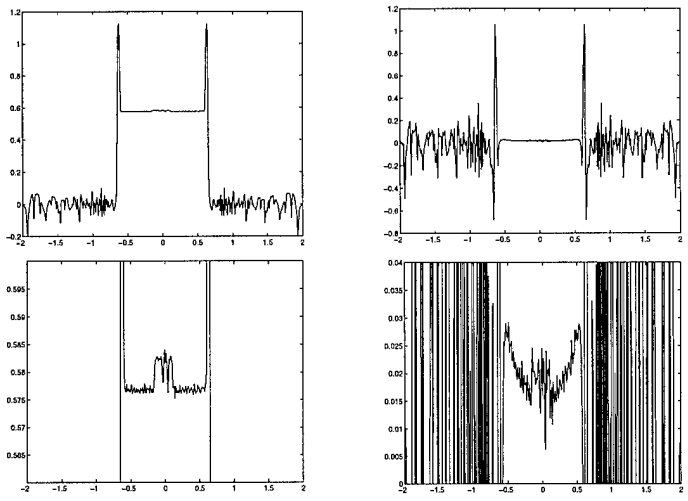

Figure 11: Cross sections corresponding to the reconstruction in Figure 6

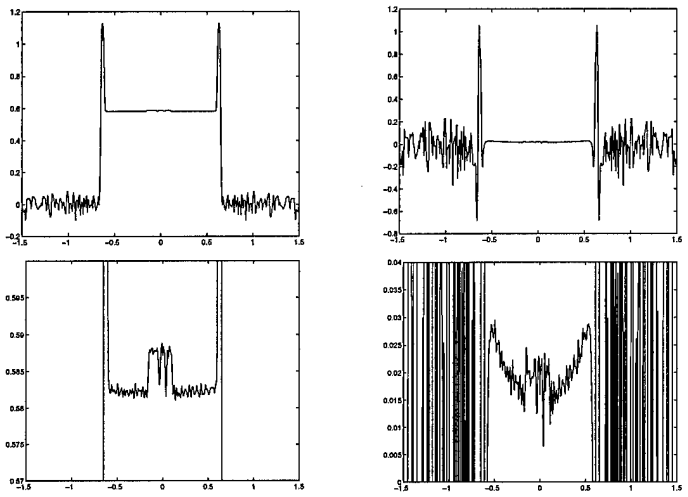

Figure 12: Cross sections corresponding to the reconstruction in Figure 7

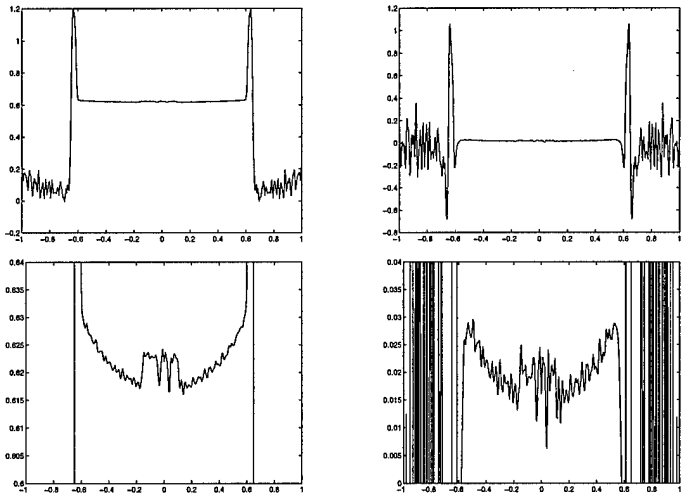

Figure 13: Cross sections corresponding to the reconstruction in Figure 8

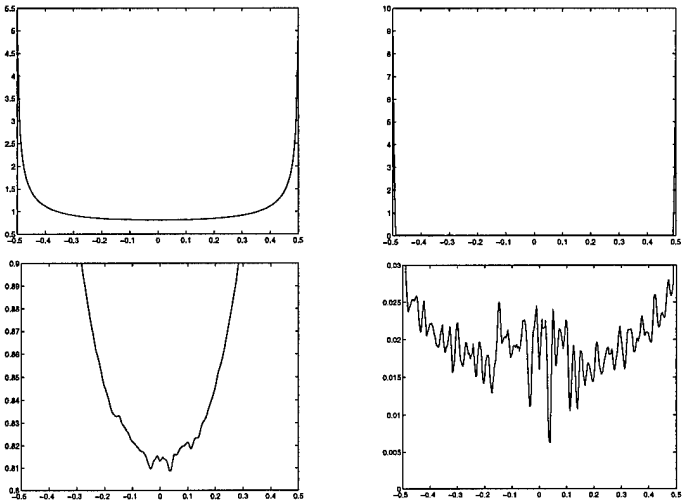

Figure 14: Cross sections corresponding to the reconstruction in Figure 9

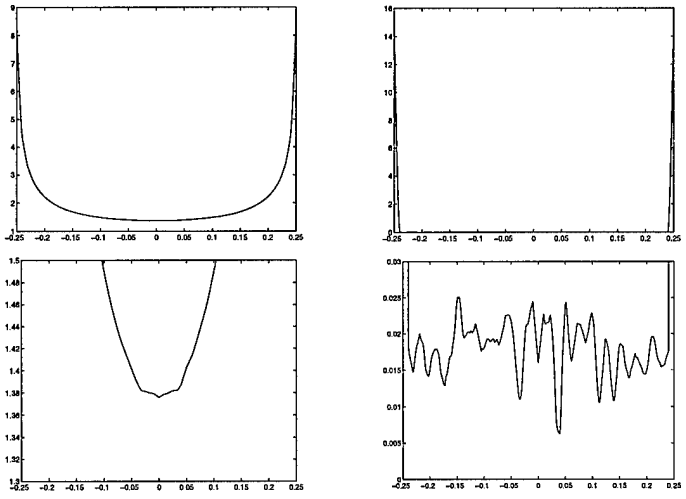

Figure 15: Cross sections corresponding to the reconstruction in Figure 10